

# Measurement of neutron production in atmospheric neutrino interactions at Super-Kamiokande

S. Han,<sup>28</sup> K. Abe,<sup>1, 49</sup> S. Abe,<sup>1, 49</sup> Y. Asaoka,<sup>1, 49</sup> C. Bronner,<sup>1</sup> M. Harada,<sup>1</sup> Y. Hayato,<sup>1, 49</sup> K. Hiraide,<sup>1, 49</sup> K. Hosokawa,<sup>1</sup> K. Ieki,<sup>1, 49</sup> M. Ikeda,<sup>1, 49</sup> J. Kameda,<sup>1, 49</sup> Y. Kanemura,<sup>1</sup> R. Kaneshima,<sup>1</sup> Y. Kashiwagi,<sup>1</sup> Y. Kataoka,<sup>1, 49</sup> S. Miki,<sup>1</sup> S. Mine,<sup>1, 7</sup> M. Miura,<sup>1, 49</sup> S. Moriyama,<sup>1, 49</sup> M. Nakahata,<sup>1, 49, 1</sup> S. Nakayama,<sup>1, 49</sup> Y. Noguchi,<sup>1</sup> G. Pronost,<sup>1</sup> K. Sato,<sup>1</sup> K. Okamoto,<sup>1</sup> H. Sekiya,<sup>1, 49</sup> H. Shiba,<sup>1</sup> K. Shimizu,<sup>1</sup> R. Shinoda,<sup>1</sup> M. Shiozawa,<sup>1, 49</sup> Y. Sonoda,<sup>1</sup> Y. Suzuki,<sup>1</sup> A. Takeda,<sup>1, 49</sup> Y. Takemoto,<sup>1, 49</sup> A. Takenaka,<sup>1</sup> H. Tanaka,<sup>1, 49</sup> T. Yano,<sup>1</sup> T. Kajita,<sup>2, 49, 23</sup> K. Okumura,<sup>2, 49</sup> R. Nishijima,<sup>2</sup> T. Tashiro,<sup>2</sup> T. Tomiya,<sup>2</sup> X. Wang,<sup>2</sup> S. Yoshida,<sup>2</sup> P. Fernandez,<sup>3</sup> L. Labarga,<sup>3</sup> N. Ospina,<sup>3</sup> D. Samudio,<sup>3</sup> B. Zaldivar,<sup>3</sup> B. W. Pointon,<sup>6, 53</sup> C. Yanagisawa,<sup>4, 35</sup> E. Kearns,<sup>5, 49</sup> J. L. Raaf,<sup>5</sup> L. Wan,<sup>5</sup> T. Wester,<sup>5</sup> J. Bian,<sup>7</sup> B. Cortez,<sup>7</sup> N. J. Grishevich,<sup>7</sup> M. B. Smy,<sup>7, 49</sup> H. W. Sobel,<sup>7, 49</sup> V. Takhistov,<sup>7, 25</sup> A. Yankelevich,<sup>7</sup> J. Hill,<sup>8</sup> M. C. Jang,<sup>9</sup> S. H. Lee,<sup>9</sup> D. H. Moon,<sup>9</sup> R. G. Park,<sup>9</sup> B. S. Yang,<sup>9</sup> B. Bodur,<sup>10</sup> K. Scholberg,<sup>10, 49</sup> C. W. Walter,<sup>10, 49</sup> A. Beauchêne,<sup>11</sup> O. Drapier,<sup>11</sup> A. Giampaolo,<sup>11</sup> A. Ershova,<sup>11</sup> Th. A. Mueller,<sup>11</sup> A. D. Santos,<sup>11</sup> P. Paganini,<sup>11</sup> C. Quach,<sup>11</sup> R. Rogly,<sup>11</sup> T. Nakamura,<sup>12</sup> J. S. Jang,<sup>13</sup> L. N. Machado,<sup>14</sup> F. P. Soler,<sup>14</sup> J. G. Learned,<sup>15</sup> K. Choi,<sup>16</sup> N. Iovine,<sup>16</sup> S. Cao,<sup>17</sup> L. H. V. Anthony,<sup>18</sup> D. Martin,<sup>18</sup> N. W. Prouse,<sup>18</sup> M. Scott,<sup>18</sup> Y. Uchida,<sup>18</sup> A. A. Sztuc,<sup>18</sup> V. Berardi,<sup>19</sup> N. F. Calabria,<sup>19</sup> M. G. Catanesi,<sup>19</sup> E. Radicioni,<sup>19</sup> A. Langella,<sup>20</sup> G. De Rosa,<sup>20</sup> G. Collazuol,<sup>21</sup> M. Feltre,<sup>21</sup> F. Iacob,<sup>21</sup> M. Mattiazzi,<sup>21</sup> L. Ludovici,<sup>22</sup> M. Gonin,<sup>23</sup> L. Périsse,<sup>23</sup> B. Quilain,<sup>23</sup> C. Fujisawa,<sup>24</sup> S. Horiuchi,<sup>24</sup> A. Kawabata,<sup>24</sup> M. Kobayashi,<sup>24</sup> Y. M. Liu,<sup>24</sup> Y. Maekawa,<sup>24</sup> Y. Nishimura,<sup>24</sup> R. Okazaki,<sup>24</sup> R. Akutsu,<sup>25</sup> M. Friend,<sup>25</sup> T. Hasegawa,<sup>25</sup> T. Ishida,<sup>25</sup> T. Kobayashi,<sup>25</sup> M. Jakku,<sup>25</sup> T. Matsubara,<sup>25</sup> T. Nakadaira,<sup>25</sup> K. Nakamura,<sup>25, 49</sup> Y. Oyama,<sup>25</sup> A. Portocarrero Yrey,<sup>25</sup> K. Sakashita,<sup>25</sup> T. Sekiguchi,<sup>25</sup> T. Tsukamoto,<sup>25</sup> N. Bhuiyan,<sup>26</sup> G. T. Burton,<sup>26</sup> F. Di Lodovico,<sup>26</sup> J. Gao,<sup>26</sup> A. Goldsack,<sup>26</sup> T. Katori,<sup>26</sup> J. Migenda,<sup>26</sup> R. M. Ramsden,<sup>26</sup> Z. Xie,<sup>26</sup> S. Zsoldos,<sup>26, 49</sup> T. Sone,<sup>27</sup> A. T. Suzuki,<sup>27</sup> Y. Takagi,<sup>27</sup> Y. Takeuchi,<sup>27, 49</sup> S. Wada,<sup>27</sup> H. Zhong,<sup>27</sup> J. Feng,<sup>28</sup> L. Feng,<sup>28</sup> J. Hikida,<sup>28</sup> J. R. Hu,<sup>28</sup> Z. Hu,<sup>28</sup> M. Kawaue,<sup>28</sup> T. Kikawa,<sup>28</sup> M. Mori,<sup>28</sup> T. Nakaya,<sup>28, 49</sup> T. V. Ngoc,<sup>28</sup> R. A. Wendell,<sup>28, 49</sup> K. Yasutome,<sup>28</sup> S. J. Jenkins,<sup>29</sup> N. McCauley,<sup>29</sup> A. Tarrant,<sup>29</sup> P. Mehta,<sup>29</sup> M. Fanì,<sup>30</sup> M. J. Wilking,<sup>30</sup> Y. Fukuda,<sup>31</sup> Y. Itow,<sup>32, 33</sup> H. Menjo,<sup>32</sup> Y. Yoshioka,<sup>32</sup> K. Ninomiya,<sup>32</sup> J. Lagoda,<sup>34</sup> S. M. Lakshmi,<sup>34</sup> M. Mandal,<sup>34</sup> P. Mijakowski,<sup>34</sup> Y. S. Prabhu,<sup>34</sup> J. Zalipska,<sup>34</sup> M. Jia,<sup>35</sup> J. Jiang,<sup>35</sup> C. K. Jung,<sup>35</sup> W. Shi,<sup>35</sup> K. Hamaguchi,<sup>36</sup> Y. Hino,<sup>36</sup> H. Ishino,<sup>36</sup> Y. Koshio,<sup>36, 49</sup> F. Nakanishi,<sup>36</sup> S. Sakai,<sup>36</sup> T. Tada,<sup>36</sup> T. Tano,<sup>36</sup> T. Ishizuka,<sup>37</sup> G. Barr,<sup>38</sup> D. Barrow,<sup>38</sup> L. Cook,<sup>38, 49</sup> S. Samani,<sup>38</sup> D. Wark,<sup>38, 44</sup> A. Holin,<sup>39</sup> F. Nova,<sup>39</sup> S. Jung,<sup>40</sup> J. Y. Yang,<sup>40</sup> J. Yoo,<sup>40</sup> J. E. P. Fannon,<sup>41</sup> L. Kneale,<sup>41</sup> M. Malek,<sup>41</sup> J. M. McElwee,<sup>41</sup> T. Peacock,<sup>41</sup> P. Stowell,<sup>41</sup> M. D. Thiesse,<sup>41</sup> L. F. Thompson,<sup>41</sup> S. T. Wilson,<sup>41</sup> H. Okazawa,<sup>42</sup> S. M. Lakshmi,<sup>43</sup> S. B. Kim,<sup>45</sup> E. Kwon,<sup>45</sup> M. W. Lee,<sup>45</sup> J. W. Seo,<sup>45</sup> I. Yu,<sup>45</sup> A. K. Ichikawa,<sup>46</sup> K. D. Nakamura,<sup>46</sup> S. Tairafune,<sup>46</sup> K. Nishijima,<sup>47</sup> A. Eguchi,<sup>48</sup> S. Goto,<sup>48</sup> S. Kodama,<sup>48</sup> Y. Mizuno,<sup>48</sup> T. Muro,<sup>48</sup> K. Nakagiri,<sup>48</sup> Y. Nakajima,<sup>48, 49</sup> S. Shima,<sup>48</sup> N. Taniuchi,<sup>48</sup> E. Watanabe,<sup>48</sup> M. Yokoyama,<sup>48, 49</sup> P. de Perio,<sup>49</sup> S. Fujita,<sup>49</sup> C. Jesús-Valls,<sup>49</sup> K. Martens,<sup>49</sup> Ll. Martí,<sup>49</sup> K. M. Tsui,<sup>49</sup> M. R. Vagins,<sup>49, 7</sup> J. Xia,<sup>49</sup> M. Kuze,<sup>50</sup> S. Izumiya,<sup>50</sup> R. Matsumoto,<sup>50</sup> K. Terada,<sup>50</sup> R. Asaka,<sup>51</sup> M. Ishitsuka,<sup>51</sup> H. Ito,<sup>51</sup> Y. Ommura,<sup>51</sup> N. Shigeta,<sup>51</sup> M. Shinoki,<sup>51</sup> M. Sugo,<sup>51</sup> M. Wako,<sup>51</sup> K. Yamauchi,<sup>51</sup> T. Yoshida,<sup>51</sup> Y. Nakano,<sup>52</sup> F. Cormier,<sup>28</sup> R. Gaur,<sup>53</sup> V. Gousy-Leblanc,<sup>53, \*</sup> M. Hartz,<sup>53</sup> A. Konaka,<sup>53</sup> X. Li,<sup>53</sup> B. R. Smithers,<sup>53</sup> S. Chen,<sup>54</sup> Y. Wu,<sup>54</sup> B. D. Xu,<sup>54</sup> A. Q. Zhang,<sup>54</sup> B. Zhang,<sup>54</sup> M. Girgus,<sup>55</sup> P. Govindaraj,<sup>55</sup> M. Posiadala-Zezaula,<sup>55</sup> S. B. Boyd,<sup>56</sup> R. Edwards,<sup>56</sup> D. Hadley,<sup>56</sup> M. Nicholson,<sup>56</sup> M. O'Flaherty,<sup>56</sup> B. Richards,<sup>56</sup> A. Ali,<sup>57, 53</sup> B. Jamieson,<sup>57</sup> S. Amanai,<sup>58</sup> D. Hamaguchi,<sup>58</sup> A. Minamino,<sup>58</sup> Y. Sasaki,<sup>58</sup> R. Shibayama,<sup>58</sup> R. Shimamura,<sup>58</sup> and S. Suzuki<sup>58</sup>

(The Super-Kamiokande Collaboration)

<sup>1</sup> Kamioka Observatory, Institute for Cosmic Ray Research, University of Tokyo, Kamioka, Gifu 506-1205, Japan

<sup>2</sup> Research Center for Cosmic Neutrinos, Institute for Cosmic Ray Research, University of Tokyo, Kashiwa, Chiba 277-8582, Japan

<sup>3</sup> Department of Theoretical Physics, University Autonoma Madrid, 28049 Madrid, Spain

<sup>4</sup> Science Department, Borough of Manhattan Community College / City University of New York, New York, New York, 1007, USA.

<sup>5</sup> Department of Physics, Boston University, Boston, MA 02215, USA

<sup>6</sup> Department of Physics, British Columbia Institute of Technology, Burnaby, BC, V5G 3H2, Canada

<sup>7</sup> Department of Physics and Astronomy, University of California, Irvine, Irvine, CA 92697-4575, USA

<sup>8</sup> Department of Physics, California State University, Dominguez Hills, Carson, CA 90747, USA

<sup>9</sup> Institute for Universe and Elementary Particles, Chonnam National University, Gwangju 61186, Korea

<sup>10</sup> Department of Physics, Duke University, Durham NC 27708, USA

<sup>11</sup> Ecole Polytechnique, IN2P3-CNRS, Laboratoire Leprince-Ringuet, F-91120 Palaiseau, France

- <sup>12</sup>Department of Physics, Gifu University, Gifu, Gifu 501-1193, Japan  
<sup>13</sup>GIST College, Gwangju Institute of Science and Technology, Gwangju 500-712, Korea  
<sup>14</sup>School of Physics and Astronomy, University of Glasgow, Glasgow, Scotland, G12 8QQ, United Kingdom  
<sup>15</sup>Department of Physics and Astronomy, University of Hawaii, Honolulu, HI 96822, USA  
<sup>16</sup>Center for Underground Physics, Institute for Basic Science (IBS), Daejeon, 34126, Korea  
<sup>17</sup>Institute For Interdisciplinary Research in Science and Education, ICISE, Quy Nhon, 55121, Vietnam  
<sup>18</sup>Department of Physics, Imperial College London , London, SW7 2AZ, United Kingdom  
<sup>19</sup>Dipartimento Interuniversitario di Fisica, INFN Sezione di Bari and Università e Politecnico di Bari, I-70125, Bari, Italy  
<sup>20</sup>Dipartimento di Fisica, INFN Sezione di Napoli and Università di Napoli, I-80126, Napoli, Italy  
<sup>21</sup>Dipartimento di Fisica, INFN Sezione di Padova and Università di Padova, I-35131, Padova, Italy  
<sup>22</sup>INFN Sezione di Roma and Università di Roma "La Sapienza", I-00185, Roma, Italy  
<sup>23</sup>ILANCE, CNRS - University of Tokyo International Research Laboratory, Kashiwa, Chiba 277-8582, Japan  
<sup>24</sup>Department of Physics, Keio University, Yokohama, Kanagawa, 223-8522, Japan  
<sup>25</sup>High Energy Accelerator Research Organization (KEK), Tsukuba, Ibaraki 305-0801, Japan  
<sup>26</sup>Department of Physics, King's College London, London, WC2R 2LS, UK  
<sup>27</sup>Department of Physics, Kobe University, Kobe, Hyogo 657-8501, Japan  
<sup>28</sup>Department of Physics, Kyoto University, Kyoto, Kyoto 606-8502, Japan  
<sup>29</sup>Department of Physics, University of Liverpool, Liverpool, L69 7ZE, United Kingdom  
<sup>30</sup>School of Physics and Astronomy, University of Minnesota, Minneapolis, MN 55455, USA  
<sup>31</sup>Department of Physics, Miyagi University of Education, Sendai, Miyagi 980-0845, Japan  
<sup>32</sup>Institute for Space-Earth Environmental Research, Nagoya University, Nagoya, Aichi 464-8602, Japan  
<sup>33</sup>Kobayashi-Maskawa Institute for the Origin of Particles and the Universe, Nagoya University, Nagoya, Aichi 464-8602, Japan  
<sup>34</sup>National Centre For Nuclear Research, 02-093 Warsaw, Poland  
<sup>35</sup>Department of Physics and Astronomy, State University of New York at Stony Brook, NY 11794-3800, USA  
<sup>36</sup>Department of Physics, Okayama University, Okayama, Okayama 700-8530, Japan  
<sup>37</sup>Media Communication Center, Osaka Electro-Communication University, Neyagawa, Osaka, 572-8530, Japan  
<sup>38</sup>Department of Physics, Oxford University, Oxford, OX1 3PU, United Kingdom  
<sup>39</sup>Rutherford Appleton Laboratory, Harwell, Oxford, OX11 0QX, UK  
<sup>40</sup>Department of Physics and Astronomy, Seoul National University, Seoul 151-742, Korea  
<sup>41</sup>Department of Physics and Astronomy, University of Sheffield, S3 7RH, Sheffield, United Kingdom  
<sup>42</sup>Department of Informatics in Social Welfare, Shizuoka University of Welfare, Yaizu, Shizuoka, 425-8611, Japan  
<sup>43</sup>August Cichkowski Institute of Physics, University of Silesia in Katowice, 75 Putka Piechoty 1, 41-500 Chorzów, Poland  
<sup>44</sup>STFC, Rutherford Appleton Laboratory, Harwell Oxford, and  
Daresbury Laboratory, Warrington, OX11 0QX, United Kingdom  
<sup>45</sup>Department of Physics, Sungkyunkwan University, Suwon 440-746, Korea  
<sup>46</sup>Department of Physics, Faculty of Science, Tohoku University, Sendai, Miyagi, 980-8578, Japan  
<sup>47</sup>Department of Physics, Tokai University, Hiratsuka, Kanagawa 259-1292, Japan  
<sup>48</sup>Department of Physics, University of Tokyo, Bunkyo, Tokyo 113-0033, Japan  
<sup>49</sup>Kavli Institute for the Physics and Mathematics of the Universe (WPI), The University of  
Tokyo Institutes for Advanced Study, University of Tokyo, Kashiwa, Chiba 277-8583, Japan  
<sup>50</sup>Department of Physics, Institute of Science Tokyo, Meguro, Tokyo 152-8551, Japan  
<sup>51</sup>Department of Physics, Faculty of Science and Technology, Tokyo University of Science, Noda, Chiba 278-8510, Japan  
<sup>52</sup>Faculty of Science, University of Toyama, Toyama City, Toyama 930-8555, Japan  
<sup>53</sup>TRIUMF, 4004 Wesbrook Mall, Vancouver, BC, V6T2A3, Canada  
<sup>54</sup>Department of Engineering Physics, Tsinghua University, Beijing, 100084, China  
<sup>55</sup>Faculty of Physics, University of Warsaw, Warsaw, 02-093, Poland  
<sup>56</sup>Department of Physics, University of Warwick, Coventry, CV4 7AL, UK  
<sup>57</sup>Department of Physics, University of Winnipeg, MB R3J 3L8, Canada  
<sup>58</sup>Department of Physics, Yokohama National University, Yokohama, Kanagawa, 240-8501, Japan

(Dated: May 2, 2025)

We present measurements of total neutron production from atmospheric neutrino interactions in water, analyzed as a function of the electron-equivalent visible energy over a range of 30 MeV to 10 GeV. These results are based on 4,270 days of data collected by Super-Kamiokande, including 564 days with 0.011 wt% gadolinium added to enhance neutron detection. The measurements are compared to predictions from neutrino event generators combined with various hadron-nucleus interaction models, which consist of an intranuclear cascade model and a nuclear de-excitation model. We observe significant variations in the predictions depending on the choice of hadron-nucleus interaction model. We discuss key factors that contribute to describing our data, such as in-medium effects in the intranuclear cascade and the accuracy of statistical evaporation modeling.

\* also at University of Victoria, Department of Physics and Astron-

omy, PO Box 1700 STN CSC, Victoria, BC V8W 2Y2, Canada.

114

## I. INTRODUCTION

115 A large fraction of neutrino experiments rely on nuclear  
 116 targets, yet significant uncertainties remain regarding the influence of nucleon correlations on interaction cross sections and particle kinematics. Modeling these “nuclear effects” is particularly critical for GeV-scale neutrino experiments aiming to measure neutrino oscillation parameters, including CP violation and mass ordering.

122 Outgoing hadrons serve as valuable probes of these effects, with recent advancements in neutrino detectors enabling precise measurements of hadron multiplicities and kinematics. For instance, proton measurements in neutrino-argon interactions have revealed discrepancies between observed and predicted kinematic distributions [1]. However, detecting neutrons in tracking detectors is challenging due to the limited detection efficiency from the small ( $n, p$ ) reaction cross section [2, 3]. This issue is crucial, as inaccuracies in estimating the “missing energy” carried by neutrons can bias key measurements, such as the Dirac CP phase [4].

134 Neutrons with kinetic energies of a few MeV or lower tend to thermalize and can be detected via the radioactive neutron capture ( $n, \gamma$ ) reactions with well-defined timescales and energy signatures, enabling clean signal selection with virtually no energy threshold. Historically, this made neutrons effective tags for antineutrino charged-current (CC) interactions (e.g.,  $\bar{\nu}_e p \rightarrow e^+ n$ ) compared to neutrino interactions (e.g.,  $\nu_e n \rightarrow e^- p$ ) [5]. Neutron tagging remains relevant today, for instance, in atmospheric neutrino oscillation analyses, where it enhances sensitivity to both neutrino mass ordering and CP violation, by preventing the cancellation of opposite-sign effects in neutrino and antineutrino oscillation probabilities [6]. It also helps suppress atmospheric neutrino backgrounds in searches for rare events, such as proton decay (e.g.,  $p \rightarrow e^+ \pi^0$  [7]), which in many cases is not expected to produce neutrons, or inverse beta decay ( $\bar{\nu}_e p \rightarrow e^+ n$ ) induced by supernova  $\bar{\nu}_e$ , which emits only one neutron.

152 Accurate prediction detectable neutrons is essential and requires well-constrained uncertainties. The modeling approach commonly adopted by GeV-scale neutrino experiments is illustrated in Figure 1. Neutrino event generators sample outgoing hadrons from the initial neutrino interaction, either at the nucleon or quark level, and subsequently model intranuclear hadron transport (often referred to as final-state interactions, or FSI), followed by nuclear de-excitation. Similarly, particle transport codes such as Geant4 [8–10] simulate hadron transport and nuclear de-excitation to describe downstream hadron interactions within the detector.

164 Accurately modeling secondary neutron production is particularly important. For hadron transport in the  $O(0.1\text{--}1)$  GeV energy range, Intranuclear Cascade (INC) models [11] are commonly used. Subsequent nuclear de-excitation involves an evaporation process that releases

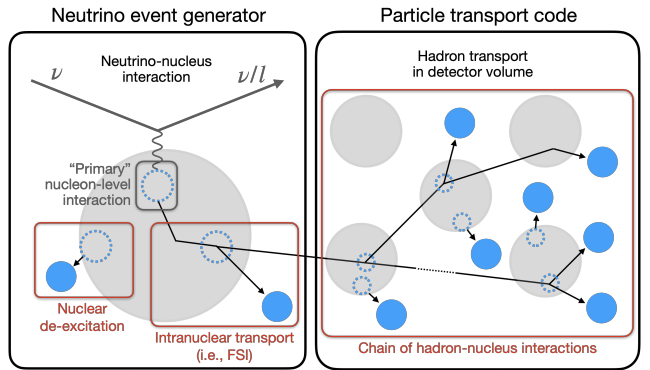


FIG. 1. Schematic illustration of nucleon production mechanisms in a typical GeV-scale neutrino interaction simulation. Black arrows indicate nucleon trajectories; solid blue circles represent detectable nucleons ejected from nuclei, while dashed blue circles denote resulting nucleon holes.

neutrons with kinetic energies of a few MeV and also contributes significantly to total neutron production. Variations in how these models account for nuclear effects often lead to significant discrepancies in predictions [12]. Several studies have measured neutron production from atmospheric or artificial neutrino interactions using water (T2K [13]), heavy water (SNO [14]), and hydrocarbon (MINERvA [2, 15], KamLAND [16]) as target materials. Several of these studies [2, 13, 15] reported deficits in observed neutron signals compared to predictions from neutrino event generators, with the discrepancies often attributed to the inaccuracy of hadron transport models.

In this paper, we present a measurement of neutron production following atmospheric neutrino interactions in water. Using data collected by the Super-Kamiokande (SK) detector from 2008 to 2022, we evaluated the average multiplicity of ( $n, \gamma$ ) reactions (“neutron captures”) as a function of electron-equivalent visible energy, a calorimetric proxy for neutrino momentum transfer. The results were compared with predictions from various models relevant to secondary neutron production. This study focuses on an event sample with visible energy greater than 30 MeV, distinct from our previous neutron measurement [17] targeting neutral-current quasi-elastic (NCQE) events with visible energy below 30 MeV.

This paper is structured as follows. Section II provides a brief overview of the SK detector. The selection process for atmospheric neutrino events and neutron signals, along with the estimation of selection performance, are detailed in Sections III and IV. Section V outlines the methodology for determining the average ( $n, \gamma$ ) multiplicity per visible energy bin and the associated systematic uncertainties. Section VI introduces the interaction models used for generating predictions. Finally, Sections VII and VIII present a comparison of observations with predictions and discuss the implications of the results.

TABLE I. SK operational phases and neutron-related characteristics. SK-IV, V, VI data were used in this analysis.

Phase	Years	Livetime [days]	Gd concentration <sup>a</sup> [wt%]	Expected $(n, \gamma)$ fraction <sup>b</sup> $H(n, \gamma)$ [%]	$Gd(n, \gamma)$ [%]	$(n, \gamma)$ time constant <sup>c</sup> [ $\mu$ s]
SK-I-III	1996–2008	2805.9	-	>99.9	-	No data
SK-IV	2008–2018	3244.4	-	>99.9	-	$204.8 \pm 9.8$
SK-V	2019–2020	461.0	-	>99.9	-	$199.8 \pm 10.2$
SK-VI	2020–2022	564.4 <sup>d</sup>	$0.0110 \pm 0.0001$ [19]	$56.1 \pm 1.5$	$43.9 \pm 1.5$	$116.2 \pm 2.3$
SK-VII-VIII	2022–present	-	$0.0332 \pm 0.0002$ [20]	$29.7 \pm 0.7$	$70.3 \pm 0.7$	$61.8 \pm 0.1$ [20]

<sup>a</sup> Based on the amount of dissolved Gd.

<sup>b</sup> Based on the evaluated thermal  $(n, \gamma)$  reaction cross sections and uncertainties of ENDF/B-VII.1 [18].

<sup>c</sup> Weighted mean of all Am/Be neutron source measurements, explained in Section IV B.

<sup>d</sup> Excludes earlier runs which showed signs of non-uniform Gd concentration, i.e., varying time constant by position.

## 205 II. THE SUPER-KAMIOKANDE DETECTOR

206 Super-Kamiokande (SK) [21] is an underground water  
 207 Cherenkov detector located in Gifu, Japan. It consists of  
 208 two optically separated, concentric cylindrical volumes:  
 209 the inner detector (ID) containing 32.5 ktons of water  
 210 and equipped with 11,129 inward-facing photomultiplier  
 211 tubes (PMTs) and the outer detector (OD) serving as  
 212 a cosmic-ray veto. The detector registers a PMT sig-  
 213 nal with a pulse height greater than 0.25 photoelectron-  
 214 equivalent charge as a “hit.” If the number of ID or OD  
 215 PMT hits within a 200-ns sliding time window ( $N_{200\text{-ns}}$ )  
 216 exceeds a given threshold, an event trigger is issued. The  
 217 details of the detector can be found in [21, 22].

218 Charged particles, namely electrons and muons pro-  
 219 duced by charged-current neutrino interactions, are iden-  
 220 tified through Cherenkov radiation. The radiation is pro-  
 221 jected onto the PMTs as a characteristic ring pattern  
 222 that depends on the particle type and energy. This ring  
 223 pattern serves as the basis for particle reconstruction.  
 224 Neutrons are indirectly identified via Compton-scattered  
 225 electrons resulting from  $(n, \gamma)$  reactions. In pure water,  
 226 most occur on  $^1\text{H}$ , emitting a single 2.2 MeV  $\gamma$ -ray. With  
 227 the recent addition of gadolinium (Gd), a large fraction  
 228 of neutrons are expected to be captured by Gd isotopes,  
 229 resulting in a total  $\gamma$ -radiated energy of around 8 MeV.

230 The  $O(1)$  MeV signal identification performance is sig-  
 231 nificantly influenced by variations in detector character-  
 232 istics. Parameters such as individual PMT gain, tim-  
 233 ing properties, quantum efficiency, and optical absorption  
 234 and scattering in water are continuously monitored using  
 235 cosmic-ray muons and light sources [22]. Additionally,  
 236 the uncertainty in Cherenkov ring energy reconstruc-  
 237 tion (described in Section III B) is evaluated over a wide en-  
 238 ergy range using naturally occurring particles, including  
 239 cosmic-ray muons, Michel electrons, and neutral pions  
 240 produced in neutral-current (NC) atmospheric neutrino  
 241 interactions in water. Figure 2 illustrates the agreement  
 242 between data and simulation in energy reconstruction for  
 243 the Gd-loaded SK-VI phase, which is mostly within 2%  
 244 across the  $O(10\text{--}10^4)$  MeV range and consistent with the  
 245 pure water phase results reported in [6].

246 The detector has operated through eight different  
 247

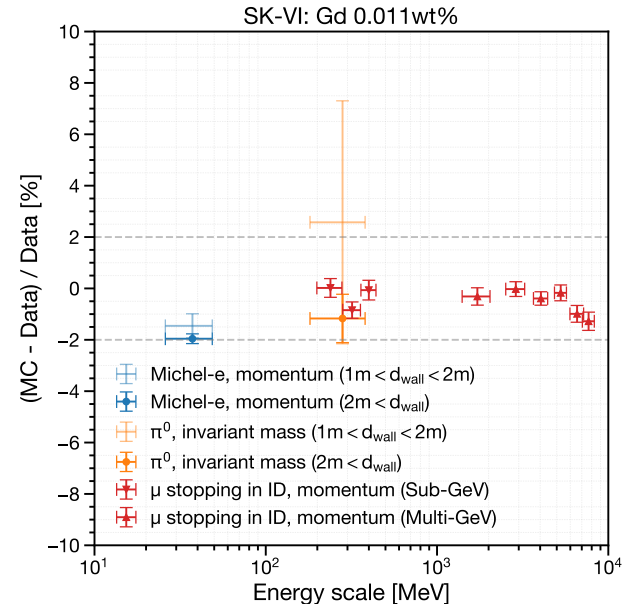


FIG. 2. Comparison of energy reconstruction performance between Monte Carlo (MC) simulation and observed data for naturally occurring particles in the Gd-loaded SK-VI phase. The variable  $d_{\text{wall}}$  represents the distance (in meters) from the reconstructed vertex to the nearest ID photodetector wall. The fiducial volume for this study is defined as  $d_{\text{wall}} > 1$  m.

phases. Neutron detection began with the fourth phase SK-IV, following the electronics upgrade [23] that allowed extended event recording up to 535  $\mu$ s after certain ID triggers. This has enabled analysis of delayed neutron captures that occur with a time scale of  $O(10\text{--}100)$   $\mu$ s following an atmospheric neutrino interaction. Between SK-IV and SK-V, in 2018, the detector underwent refurbishment, during which malfunctioning PMTs were replaced. The later phases, SK-VI, SK-VII, and SK-VIII involved the dissolution of  $\text{Gd}_2(\text{SO}_4)_3$  into the water volume to enhance neutron detection efficiency [19, 20]. Table I summarizes the relevant operational conditions.

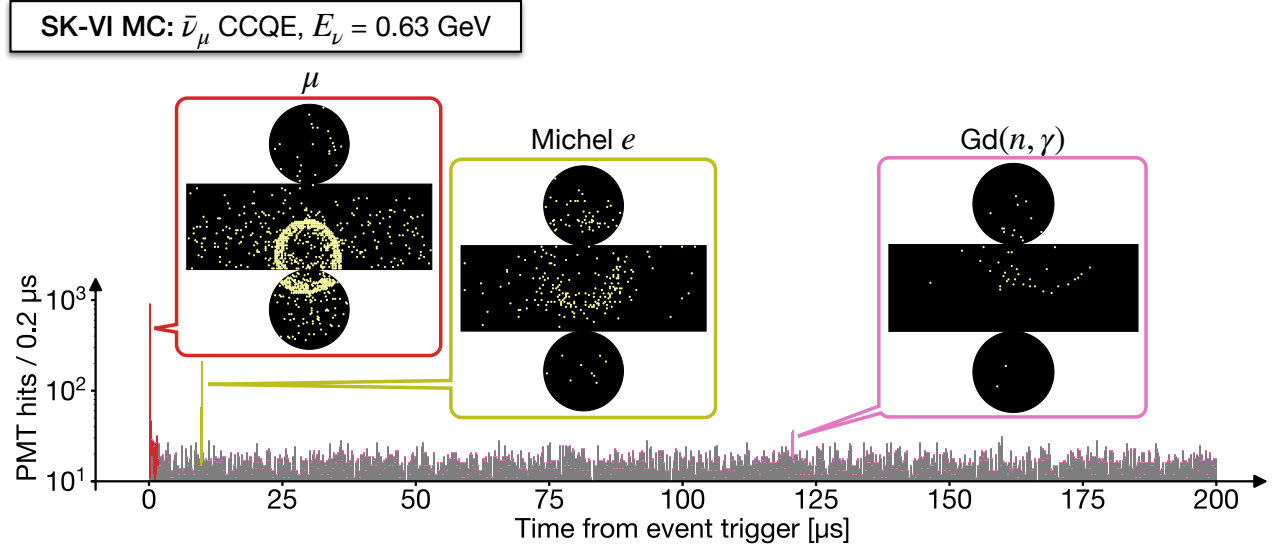


FIG. 3. A PMT hit time distribution for a typical  $\bar{\nu}_\mu$  charged-current (CC) quasi-elastic (QE) interaction with a muon and a neutron as final states. The zero is set at the event trigger. The event displays feature the “prompt” muon signal (red) and the two types of “delayed” coincident signals — Michel electrons from muon decay (olive) and neutron captures on Gd (pink). The gray bars represent randomly recorded background PMT hits. This event was simulated in the SK-VI configuration.

### 260 III. ATMOSPHERIC NEUTRINO EVENTS

#### 261 A. Event selection

262 We followed a typical selection process for atmospheric  
263 neutrino interactions that are fully contained within the  
264 ID, similar to previous studies conducted at SK [6]. All  
265 events were required to pass the ID trigger with the  
266 threshold  $N_{200\text{-ns}} \geq 58$  PMT hits—roughly correspond-  
267 ing to a 10 MeV electron—followed by the extended event  
268 window of 535  $\mu\text{s}$  for neutron detection. Background  
269 events from cosmic-ray muons, radioactivity, and neu-  
270 trino interactions with exiting particles were reduced us-  
271 ing OD veto and ID charge cuts.

272 Selected events were reconstructed as described in Sec-  
273 tion III B. To further reject low-energy backgrounds, we  
274 required that the reconstructed vertex be more than 1  
275 m away from the ID tank wall (defining the fiducial vol-  
276 ume with 27.2 kton of water) and that the visible energy  
277 be larger than 30 MeV. The remaining background con-  
278 tamination, mainly due to cosmic-ray muons stopping in  
279 the ID and PMT discharges, was estimated to be below  
280 0.2%, based on visual inspection [7].

#### 281 B. Reconstruction of prompt Cherenkov rings

282 Figure 3 shows a simulated PMT hit time distribution  
283 of a typical  $\bar{\nu}_\mu$  charged-current (CC) quasi-elastic (QE)  
284 event followed by a Michel electron and a  $\text{Gd}(n, \gamma)$  re-  
285 action, along with the corresponding event displays. For  
286 the “prompt” radiation due to charged particles (namely,  
287

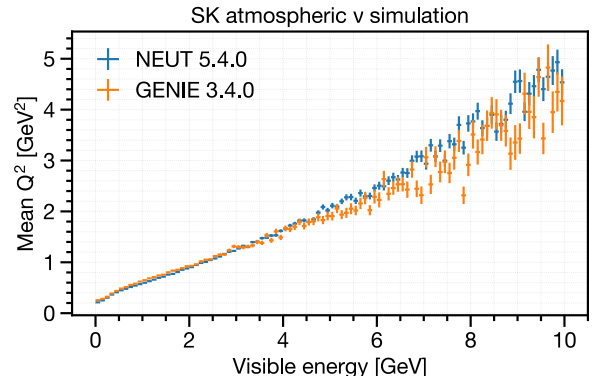


FIG. 4. Average squared momentum transfer ( $Q^2$ ) per visible energy bin for simulated atmospheric neutrino events at SK, compared between two different neutrino event genera-  
tors. NEUT 5.4.0 (blue) uses the baseline setup described in  
Section III C, while GENIE 3.4.0 [24–26] uses the “hN” setup  
as described in Section VI.

287 electrons and muons) produced via the primary neutrino  
288 interaction, we followed the Cherenkov ring reconstruc-  
289 tion process [27] as applied in previous SK analyses [6, 7].

The visible energy of an event is defined as the sum of the reconstructed kinetic energies of all Cherenkov rings, assuming each ring originates from an electron. This calorimetric measure serves as a reliable proxy for neutrino momentum transfer, as demonstrated by the positive correlation shown in Figure 4.

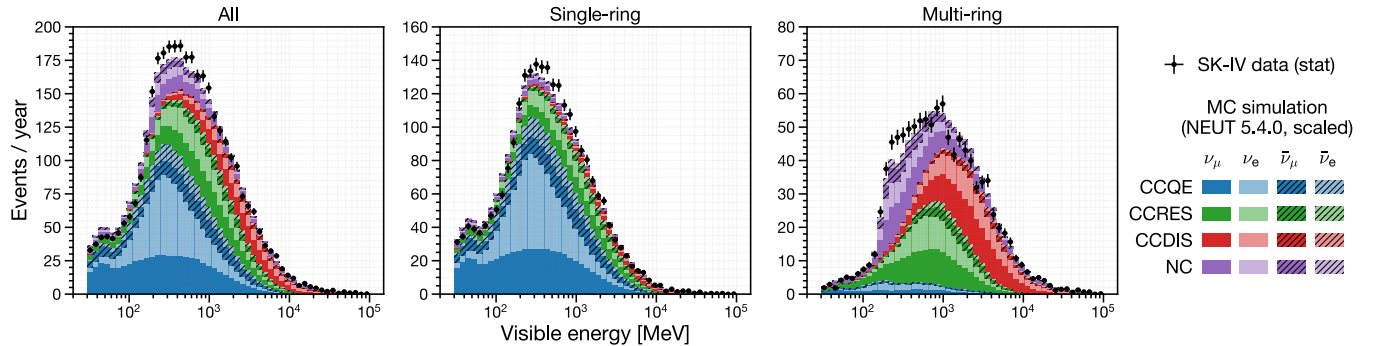


FIG. 5. Observed and simulated visible energy distributions for selected atmospheric neutrino interactions, for the longest SK-IV phase: all events (left), events with one reconstructed Cherenkov ring (middle), and events with two or more rings (right). CCQE events dominate the single-ring sample, while CCRES and CCDIS events dominate the multi-ring sample. NC events in the multi-ring sample are mostly RES or DIS interactions. The simulation setup is detailed in Section III C. Simulated distributions are scaled to match the SK-IV data to account for the uncertainty in absolute neutrino flux normalization.

296

### C. Baseline simulation setup

The simulation of atmospheric neutrino events involves<sup>336</sup> a convolution of the atmospheric neutrino flux, neutrino<sup>337</sup> event generator, and detector simulation.<sup>338</sup>

To determine the incoming neutrino kinematics and<sup>339</sup> event rate, we used atmospheric flux calculations for  $\nu_e$ ,<sup>340</sup>  $\nu_\mu$ ,  $\bar{\nu}_e$ , and  $\bar{\nu}_\mu$  at the detector site, assuming no oscillations,<sup>341</sup> as provided by Honda *et al.* [28] for  $[10^2, 10^7]$  MeV<sup>342</sup> range. Neutrinos with energies below 100 MeV, as well as<sup>343</sup> the  $\nu_\tau$  and  $\bar{\nu}_\tau$  interactions, were neglected as their overall<sup>344</sup> presence in data is expected to be small.<sup>345</sup>

Neutrino interactions in water were modeled using neutrino<sup>346</sup> event generators [29], which compute the cross sec-<sup>347</sup> tions for each interaction channel and sample outgoing<sup>348</sup> particle kinematics. NEUT 5.4.0 [30] was used as the<sup>349</sup> baseline event generator. It covers major interaction<sup>350</sup> channels, including QE scattering with single (1p1h) or<sup>351</sup> double (2p2h) nucleon knockout, single pion production<sup>352</sup> due to  $\Delta$  resonance (RES), and multiple pion produc-<sup>353</sup> tion via deep inelastic scattering (DIS). The models used<sup>354</sup> are consistent with the latest SK atmospheric neutrino<sup>355</sup> oscillation analysis [6]. The transport of hadronic final<sup>356</sup> states within the target nucleus (FSI) was modeled sepa-<sup>357</sup>rately from the primary neutrino interaction. The trans-<sup>358</sup>port of low-momentum ( $< 500$  MeV/c) pions was based<sup>359</sup> on Salcedo *et al.* [31], with parameters tuned to fit ex-<sup>360</sup>ternal pion-nucleus scattering data [32]. For higher en-<sup>361</sup>ergy nucleons and pions, FSIs were modeled using the<sup>362</sup> INC approach, which includes elastic scattering and sin-<sup>363</sup>gle/double pion production. The cross sections for reac-<sup>364</sup>tions with free target nucleons were sourced from Bertini<sup>365</sup> [33] for nucleon projectiles and from external pion scat-<sup>366</sup>tering data for high-momentum pion projectiles [34]. The<sup>367</sup> de-excitation of an oxygen target was modeled using tab-<sup>368</sup>ulated occupation probabilities for nucleon energy states<sup>369</sup> [35] and branching ratios for knockout of each state [36].<sup>370</sup>

The subsequent particle transport in water and detec-<sup>370</sup>tor responses were simulated using GCALOR [37] cou-<sup>371</sup>

pled with GEANT 3.21 [38]. Propagation of nucleons and charged pions below 10 GeV was simulated based on the Bertini cascade model [39]. For cross sections, GCALOR uses ENDF/B-VI [40] for low-energy (below 20 MeV, or 195 MeV/c in momentum) neutrons, and Bertini-based tabulation [39] for the remaining nucleons and charged pions. The transport of low-momentum pions was separately modeled using the NEUT pion FSI routine to ensure consistency between NEUT and GEANT.

For the transport of low-energy neutrons in the Gd-loaded SK-VI phase, we imported reaction cross sections from the Geant4.10.5.p01 [8–10] NeutronHP database [41] based on ENDF/B-VII.1 [18], replacing ENDF/B-VI for neutron energies below 20 MeV. Additionally, we modeled the  $\gamma$ -cascade resulting from neutron captures on <sup>155/157</sup>Gd using the ANNRI-Gd model [42, 43].

The characteristics of individual PMTs and the optical parameters in water were adjusted to align with calibration data obtained from light sources and through-going cosmic-ray muons. To accurately account for detector noise, randomly recorded PMT hits were included as background, represented as gray bars in Figure 3.

500 years of atmospheric neutrino events were simulated for each SK phase and processed as described in Sections III B and III A. The events in the final sample were weighted based on the standard three-flavor oscillation probability in matter [44], using the oscillation parameters fitted with reactor constraints in the previous SK analysis [45] and the PREM model [46] for Earth’s matter density. Corrections for atmospheric neutrino flux accounting for solar activity were also applied.

Figure 5 shows the visible energy distributions of the simulated event sample. Single-ring events exhibit a higher fraction of QE interactions and a smaller fraction of DIS compared to multi-ring events. For the same visible energy, multi-ring events are expected to produce more secondary neutrons than single-ring events, due to a higher fraction of DIS interactions.

## IV. NEUTRON SIGNAL SELECTION

373 Neutrons produced by atmospheric neutrino interactions in the SK ID are primarily captured by  $^1\text{H}$  or  $^{155}/^{157}\text{Gd}$  isotopes within approximately  $O(100)$   $\mu\text{s}$ , with expected capture ratios summarized in Table I. Electrons that are scattered by the  $O(1)$  MeV  $\gamma$ -rays generate Cherenkov photons that form faint rings on the ID tank wall (hereafter referred to as “neutron signal”), as shown in Figure 3.

381 Fast neutrons, along with the subsequent  $\gamma$ -rays and scattered electrons, typically travel only a few tens of centimeters in water. Thus, signal photons can be approximated as originating from a single vertex. While reconstructing this vertex is challenging due to the limited number of PMT hits, *assuming* it to be near another known vertex, such as the reconstructed neutrino interaction vertex, helps identify signals from random PMT coincidences caused by dark current. Remaining Michel electrons from muon decays can be effectively suppressed through cuts based on signal timing and energy.

### A. Signal selection algorithm

393 The signal selection algorithm is based on Ref. [47], and consists of two stages.

395 In the first candidate search stage, we initially subtract the expected photon time-of-flight (ToF) from the individual PMT hit times for a given *assumed* signal vertex, which was provided by the reconstructed neutrino event vertex. Then, we slide a time window of 14 ns width on the ToF-corrected PMT hit times to trigger on the number of included PMT hits. The threshold was 5 for pure water phases SK-IV and V, and 7 for the Gd-loaded phase SK-VI. The search span for each event was [18, 534]  $\mu\text{s}$  from the event trigger for SK-IV–V, and [3, 534]  $\mu\text{s}$  for SK-VI with faster neutron capture time. For overlapping candidates within 50 ns, only the candidate with the largest number of PMT hits is selected.

408 In the second candidate classification stage, we extract features of each candidate and use a neural network to classify each candidate into signal and noise based on input features. These features characterize the signal energy, the background hit level, timing spread assuming the vertex, correlation between the input vertex and the hit PMT positions, correlation to the known properties of PMT noise, and angular correlation among hit PMTs relative to the Cherenkov cone opening angle.

418 The major changes from the original algorithm [47] include a simplified algorithm, a reduced set of features, and a heuristically tuned neural network architecture. These modifications aim to reduce performance bias between the data and the simulation that is used to train the neural networks.

423 Here, we provide the definition and unit of each feature used for the classification of signal candidates, along with their expected distributions as shown in Figure 6:

- **NHits**

The number of selected PMT hits within the 14-ns sliding time window.

- **NResHits**

The number of PMT hits within  $[-100, +100]$  ns from the center of the 14-ns sliding time window, minus NHits.

- **TRMS [ns]**

The root mean square (RMS) of the ToF-corrected time distribution of the selected PMT hits.

- **FitGoodness**

The normalized likelihood of the ToF-corrected time distribution of the selected PMT hits, given the *assumed* signal vertex and the Gaussian PMT timing resolution of 5 ns.

- **DWall [cm]**

The distance from the *assumed* signal vertex to the nearest tank wall.

- **DWallMeanDir [cm]**

The shorter of the radial and vertical distances from the *assumed* signal vertex to the tank wall, calculated along the average direction of the unit vectors connecting the vertex to each hit PMT.

- **BurstRatio**

The ratio of the selected PMTs with a preceding hit within 10  $\mu\text{s}$ , which are likely caused by scintillation within the irradiated PMT glass.

- **DarkLikelihood**

The normalized log likelihood ratio based on measured individual PMT dark rates, given by:

$$\text{DarkLikelihood} = \sigma \left( \log \prod_{i=1}^{\text{NHits}} \frac{r_i}{\langle r \rangle} \right) \quad (1)$$

where  $\sigma$  represents the sigmoid function,  $r_i$  is the dark rate of the  $i^{\text{th}}$  PMT, and  $\langle r \rangle$  is the average dark rate of all ID PMTs.

- **OpeningAngleStdev [deg]**

The standard deviation of the opening angles of cones formed by every possible combination of three hit PMTs and the *assumed* signal vertex.

- **Beta(k),  $k \in \{1, 2, 3, 4, 5\}$**

$$\text{Beta}(k) = \frac{2}{\text{NHits}(\text{NHits} - 1)} \sum_{i \neq j} P_k(\cos \theta_{ij}) \quad (2)$$

where  $P_k$  is the  $k^{\text{th}}$  Legendre polynomial and  $\theta_{ij}$  is the opening angle between the assumed signal vertex and the  $i^{\text{th}}$  and  $j^{\text{th}}$  hit PMTs.

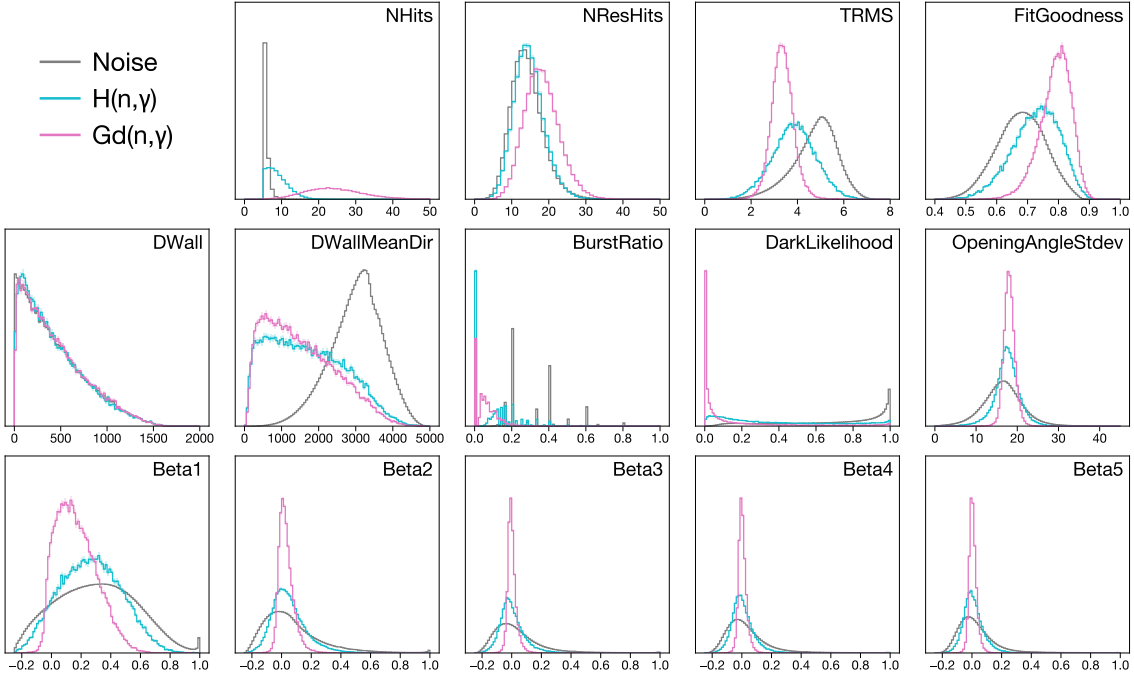


FIG. 6. The features (area-normalized) of neutron signals and noise from the thermal neutron MC simulation used for training the neural network for SK-VI phase.

For training the neural network, we utilized the features and labels of first-stage candidates from a particle-gun simulation of thermal neutrons, with vertices randomized within the ID. Each first-stage candidate, as shown in Figs. 6 and 7, was labeled as signal if it was triggered within 50 ns of the simulated  $(n, \gamma)$  reaction, and otherwise as background. Of the training dataset, 80% was used for updating the neural network weights, while the remaining 20% was reserved for validation.

We implemented a feed-forward fully connected neural network using Keras 2.6.0 [48]. The network consisted of an input layer with 14 features, followed by three dense layers, each comprising 128 ReLU-activated nodes with a 50% dropout rate, and a single sigmoid output node. Weights and biases were initialized following He *et al.* [49] and optimized by minimizing the binary cross-entropy loss iteratively on minibatches of size 2,048 using the Adam optimizer [50]. The initial learning rate was set to 0.0001. Training was stopped when signal efficiency on the validation set showed no improvement for 5 consecutive epochs. A neural network was trained for each SK phase: SK-IV, SK-V, and SK-VI.

Candidates with a neural network output greater than 0.7 were classified as signals, while those with a large number of PMT hits ( $\text{NHits} > 50$ ) and occurring earlier than the typical neutron capture timescale ( $< 20 \mu\text{s}$ ) were identified as Michel electrons and excluded. The effectiveness of this Michel electron rejection is illustrated in Figure 7. When applied to cosmic-ray muons decaying within the ID, the selection achieved an efficiency of  $98.4 \pm 1.3\%$  and a purity of  $98.7 \pm 0.5\%$ .

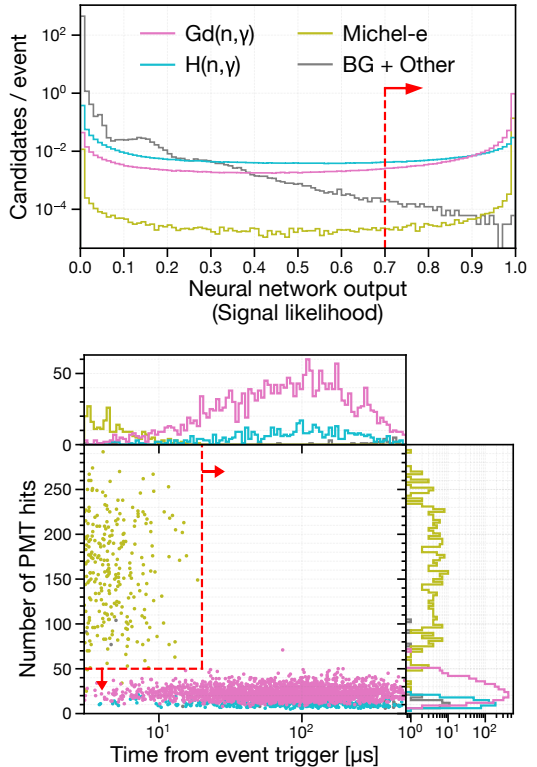


FIG. 7. The neural network response to neutron signals and backgrounds in the SK-VI atmospheric neutrino simulation (top), and the time versus energy distribution of signal candidates passing the neural network selection (bottom). Red arrows indicate the corresponding cut points.

## 500 B. Signal selection performance on calibration data

501 An Am/Be neutron source with a measured total intensity  
 502 of  $236.8 \pm 5.0$  neutrons/s [51] was used to obtain cal-  
 503 ibration data for estimating the signal detection perfor-  
 504 mance. The first excited state of the alpha-absorbed  ${}^9\text{Be}$ ,  
 505 with a roughly 60% branching ratio, emits a fast neu-  
 506 tron and a 4.44 MeV  $\gamma$ -ray simultaneously. This source  
 507 was encapsulated with Bismuth Germanate ( $\text{Bi}_4\text{Ge}_3\text{O}_{12}$ ,  
 508 BGO) crystals so that the 4.44 MeV  $\gamma$ 's can induce scin-  
 509 tillation. The setup was deployed in various positions  
 510 within the ID, and events were recorded for 30 minutes  
 511 to 1 hour. Events with a trigger charge yield correspond-  
 512 ing to the 4.44 MeV  $\gamma$ -ray scintillation were regarded as  
 513 the single neutron control sample.

514 The observed light yield distribution was compared  
 515 with dedicated simulation, as shown in Figure 8. The  
 516 simulation accounts for continuous source activity and  
 517 pile-up, by reorganizing the simulated detector response  
 518 to Am/Be neutron emission on a single global time axis,  
 519 based on the measured total neutron intensity and the es-  
 520 timated branching ratios to each excited state of alpha-  
 521 absorbed  ${}^9\text{Be}$ . As shown in Figure 8, this simulation  
 522 accurately models event triggers due to ambient neutron  
 523 captures and neutron inelastic interactions within scintil-  
 524 lator crystal. The contamination of such unwanted event  
 525 triggers in the 4.44 MeV  $\gamma$ -ray event selection was esti-  
 526 mated to be at a few percent level.

527 Within the selected events in the single neutron con-  
 528 trol sample, signal candidates were obtained following the  
 529 algorithm described in Section IV A, with the *assumed*  
 530 signal vertex set at the source position.

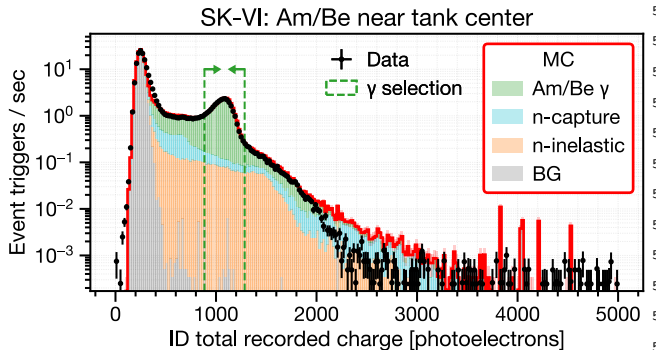


FIG. 8. Distribution of recorded charge within the time win-  
 551 dow  $[-0.5, 1.0]$   $\mu\text{s}$  relative to event triggers, measured with  
 552 an Am/Be neutron source positioned near the ID tank cen-  
 553 ter. The black points represent SK-VI data, while the red line  
 554 shows the simulated prediction. The green dashed arrows in-  
 555 dicate the selection window for 4.44 MeV  $\gamma$ -ray-induced scin-  
 556 tillation. Roughly 95% of the selected events are attributed  
 557 to  $\gamma$ 's from the Am/Be source (green), with the remaining  
 558 5% arising from ambient neutron captures (blue) and neu-  
 559 trons inelastically producing charged particles in the scintil-  
 560 lator (orange). The contribution from background events (la-  
 561 beled "BG," gray) is negligible. The pink shades indicate MC  
 562 statistical errors.

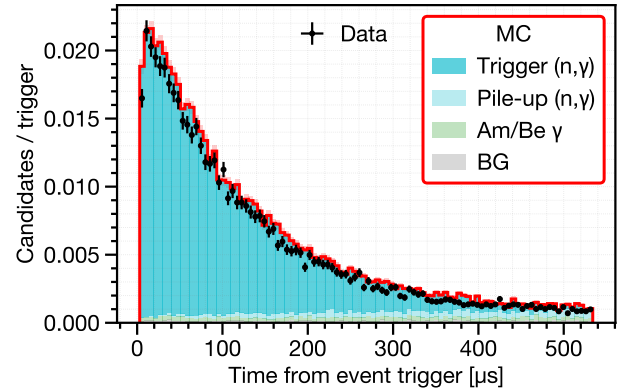


FIG. 9. Exponential decrease of the selected neutron signal candidates as a function of the time from the selected event triggers with the Am/Be neutron source positioned near the ID tank center, in the SK-VI phase. The label "Trigger ( $n, \gamma$ )" indicates captures of neutrons produced within 350 ns from the event trigger, while the label "Pile-up ( $n, \gamma$ )" indicates captures of piled-up neutrons without such correlation to the event trigger. The pink shades indicate MC statistical errors.

Figure 9 shows an example time distribution of the selected signal candidates. Such distributions of the time  $t$  were fitted with a function  $f$  of the form:

$$f(t) = A(1 - e^{-t/\tau_{\text{thermal}}})e^{-t/\tau_{\text{capture}}} + B \quad (3)$$

where the normalization constant  $A$ , the background constant  $B$ , the neutron thermalization time scale  $\tau_{\text{thermal}}$ , and the neutron capture time constant  $\tau_{\text{capture}}$  are free parameters. The signal efficiency was evaluated as the number of identified signals per selected event triggers, corrected by the constant background term  $B$ . Figure 10 shows the estimated neutron detection efficiencies for various source positions in the ID.

The major sources of systematic uncertainty are summarized in Table II. In the pure water phases (SK-IV and V), the dominant source of uncertainty lies in the potential bias caused by the calibration setup, such as the unwanted event triggers or time correlation of false positives to event triggers, often leading to an overestimation of the background constant  $B$ . The size of this uncertainty was conservatively estimated by comparing the true and estimated signal efficiencies from the simulations and quantifying the fluctuation within each SK phase. In the Gd-loaded phase (SK-VI), the dominant source of uncertainty is in the fraction and the  $\gamma$  emission model of the  $Gd(n, \gamma)$  reaction. The size of these uncertainties is estimated based on the evaluated thermal neutron capture cross section uncertainties in ENDF/B-VII.1, as well as variations in the estimated signal efficiency when using an alternative photon strength function to describe the Gd continuum  $\gamma$ -cascade in the ANNRI-Gd model [42].

The discrepancy between observed and predicted signal efficiencies in SK-VI (Figure 10) likely arises from an

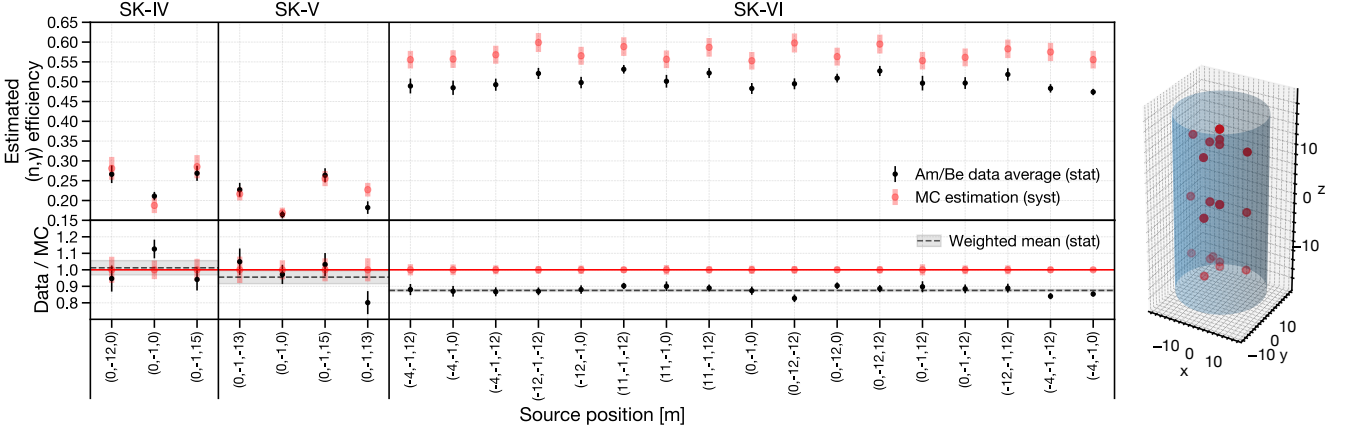


FIG. 10. Estimated  $(n, \gamma)$  signal selection efficiencies for each calibration position within the tank (red markers in the schematic on the right). For SK-VI positions with multiple measurements taken on different dates, the reported efficiency is the average of those measurements. Systematic uncertainties considered in the MC simulation are summarized in Table II.

TABLE II. Major sources of systematic uncertainty in the neutron detection efficiency estimated with the Am/Be neutron source. <sup>586</sup>

Source	SK-IV	SK-V	SK-VI
Am/Be neutron characterization	0.5% <sup>589</sup>	0.9% <sup>590</sup>	0.5% <sup>589</sup>
Detector response	2.2%	3.3%	1.2% <sup>590</sup>
Bias due to calibration setup	6.9%	4.6%	1.1%
Gd( $n, \gamma$ ) fraction	-	-	2.1%
Gd( $n, \gamma$ ) $\gamma$ emission model	-	-	2.6% <sup>591</sup>
Total	7.3%	5.7%	3.8% <sup>591</sup>

## V. $(n, \gamma)$ MULTIPLICITY ESTIMATION

The average multiplicity of total  $(n, \gamma)$  reactions is computed as the average of the expected number of  $(n, \gamma)$  reactions estimated on an event-by-event basis, as follows:

$$\langle N \rangle = \left\langle \frac{N_i^{\text{detected}} - N_i^{\text{BG}}}{\epsilon_i} \right\rangle \quad (4)$$

Here,  $N_i^{\text{detected}}$  is the count of detected signals,  $N_i^{\text{BG}}$  is the estimated number of false positives, and  $\epsilon_i$  is the estimated signal detection efficiency of the  $i^{\text{th}}$  event.

Accurate estimation of  $N_i^{\text{BG}}$  and  $\epsilon_i$  is crucial. While Am/Be calibration data provides a basis for these estimates, additional factors in atmospheric neutrino events—such as neutrino vertex reconstruction accuracy and larger neutron kinetic energy—may significantly impact the signal selection performance. To better account for these effects in the calculation of  $N_i^{\text{BG}}$  and  $\epsilon_i$ , we trained Generalized Additive Models (GAMs) [55] on the baseline atmospheric neutrino simulations. Using pyGAM 0.9.0 [56], a total of six linear GAMs were constructed across the three SK phases, for two output metrics: signal selection efficiency and false positive rate.

Using the baseline MC simulation generated with NEUT 5.4.0, GAMs were fitted to the simulated distributions of each metric, averaged within bins in a five-dimensional feature space. The features consist of reconstructed neutrino event variables, including visible energy, Cherenkov ring multiplicity, the particle type of the most energetic ring, and the radial and vertical displacements of the neutrino interaction vertex. No assumptions were made regarding feature correlations, and appropriate smoothing was applied to mitigate overfitting. The  $1\sigma$  prediction interval was determined based on the MC statistical uncertainties within each bin.

overestimation of the Gd( $n, \gamma$ ) fraction in Geant4 [52, 53] <sup>594</sup>. For example, the Gd( $n, \gamma$ ) fraction estimated using SK- VI Am/Be data was  $(44 \pm 3)\%$  [52], consistent with the <sup>595</sup>  $(43.9 \pm 1.5)\%$  evaluated with thermal neutron capture <sup>596</sup> cross sections in ENDF/B-VII.1 [54], yet both were lower <sup>597</sup> than the 52% predicted by Geant4.10.5.p01 NeutronHP <sup>598</sup> using the same cross sections. This problem with Geant4 <sup>599</sup> is attributed to its treatment of hydrogen as free rather <sup>600</sup> than bound in water molecules, leading to an underesti- <sup>601</sup> mation of the competing  ${}^1\text{H}(n, \gamma)$  reaction [53]. <sup>602</sup>

To address this discrepancy, we applied a correction <sup>603</sup> based on the weighted mean of Am/Be data-to-MC ef- <sup>604</sup> ficiency ratios across all source positions. Signal effi- <sup>605</sup> ciencies in the pure water phases with limited calibra- <sup>606</sup> tion data were further corrected to ensure consistency <sup>607</sup> in the overall neutron counts with the well-calibrated <sup>608</sup> Gd-loaded phase, and the final correction factors were <sup>609</sup>  $0.90 \pm 0.12$  (SK-IV),  $0.94 \pm 0.04$  (SK-V), and  $0.88 \pm 0.01$  <sup>610</sup> (SK-VI) (see Appendix A for details). <sup>611</sup>

The measured  $\tau_{\text{capture}}$  in Equation 3 were  $200.4 \pm 3.7$   $\mu\text{s}$  <sup>612</sup> (pure water, SK-IV and SK-V combined) and  $116.9 \pm 0.3$   $\mu\text{s}$  <sup>613</sup> (Gd-loaded, SK-VI), consistent with ENDF/B-VII.1 <sup>614</sup> predictions of  $204.7 \pm 5.3$   $\mu\text{s}$  and  $114.9 \pm 2.5$   $\mu\text{s}$ . <sup>615</sup>

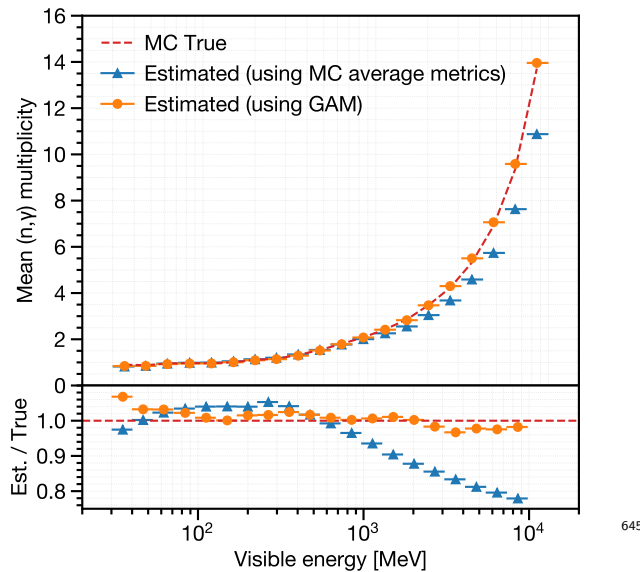


FIG. 11. The true (dashed lines) and estimated average (648) ( $n, \gamma$ ) multiplicity (circle markers: using GAM, triangle markers: using the overall average signal efficiency and false positive rate obtained from the given simulation) as a function (649) of visible energy, for the test simulations of atmospheric neutrino events produced with NEUT 5.1.4. (650)

Trained GAMs were tested on a simulation using (655) NEUT 5.1.4, which predicts roughly 10% lower (656) ( $n, \gamma$ ) multiplicity overall. Figure 11 shows the performance (657) of the trained GAM in estimating the true average signal (658) multiplicity per visible energy bin. By reconstructing (659)  $N_i^{\text{BG}}$  and  $\epsilon_i$  on an event-by-event basis, the GAM helps (660) reduce potential biases in the results, particularly in the (661) multi-GeV bins.

The following major systematic uncertainties affecting (663) signal counting were evaluated on a bin-by-bin basis for (664) each operational phase and data subsample:

### (1) Overall signal efficiency scale

This includes calibration uncertainties (Section IV B) (668) and phase-dependent variations (to be explained in (669) Appendix A).

### (2) Signal selection performance modeling (GAM)

This is quantified as the difference between true and (673) estimated signal multiplicities in simulations. The ratio (674) is also used to correct the estimated distribution.

### (3) Neutrino event reconstruction

This assumes 2% visible energy resolution (Figure 2), (678) with ring-counting errors accounted for single- and (679) multi-ring events.

Figure 12 shows fractional uncertainties per visible energy (682) bin for the full data sample. The largest uncertainty (683) lies in the overall signal efficiency scale and statistics.

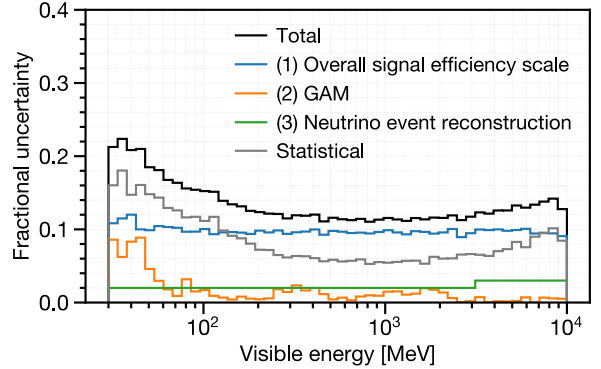


FIG. 12. Fractional uncertainties assigned to the estimated average ( $n, \gamma$ ) multiplicity per bin for the full data sample.

## VI. TESTED MODELS

To compare with data, we generated predictions for the average ( $n, \gamma$ ) multiplicity as a function of neutrino event visible energy using various neutrino event generators and hadron-nucleus interaction models. Six generator configurations were tested: NEUT 5.4.0, NEUT 5.6.3, GENIE hA, GENIE hN, GENIE BERT, and GENIE INCL. The GENIE setups use GENIE 3.4.0 with G\_18a\_10x\_02\_11b physics tunes [26], where  $x \in \{a, b, c, d\}$  corresponds to the FSI model: INTRANUKE/hA [25] (hA), INTRANUKE/hN [25] (hN), the Geant4 Bertini cascade model [57] (BERT), and the Liège INC model [58] (INCL).

NEUT 5.4.0 follows the setup described in Section III C, while NEUT 5.6.3 includes a modified nuclear binding energy, removing roughly 10% of QE interactions in which the struck nucleon falls below the revised threshold. The GENIE setups share QE and single-pion production models with NEUT but differs in FSI and hadronization. Except for GENIE hA, all FSI models use the full INC approach. Also, the Liège INC model in GENIE is coupled with ABLA07 [59] for nuclear de-excitation.

Secondary hadron-nucleus interaction models were tested using SK detector simulations with GEANT 3.21 and Geant4.10.5.p01, in six configurations: SK-IV/V default, SK-VI default, G3 GCALOR, G4 BERT, G4 BERT\_PC, and G4 INCL\_PC. The SK-IV/V and SK-VI setups differ mainly in neutron reaction cross sections below 20 MeV, using ENDF/B-VI and ENDF/B-VII.1, respectively. G3 GCALOR relies entirely on GCALOR within GEANT 3.21, while the baseline setups use the NEUT pion FSI routine. Geant4-based models adopt ENDF/B-VII.1 for low-energy neutron transport, with G4 BERT and G4 BERT\_PC using the Bertini cascade, and G4 INCL\_PC using the Liège INC model. Configurations with the PC suffix employ the Geant4 Precompound model [60] for nuclear de-excitation, while G4 BERT uses a simpler native model [57]. GEANT-3-based models rely on Bertini-based tabulation [39] for hadron-nucleus cross sections (excluding low-energy neutrons), whereas Geant4-based models use Glauber parameterization [61].

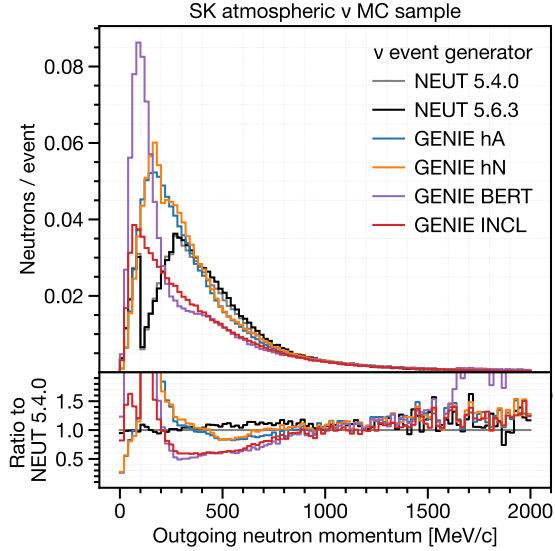


FIG. 13. Comparison of neutrino event generator options with different FSI models: Outgoing neutron momentum distribution per selected atmospheric neutrino event.

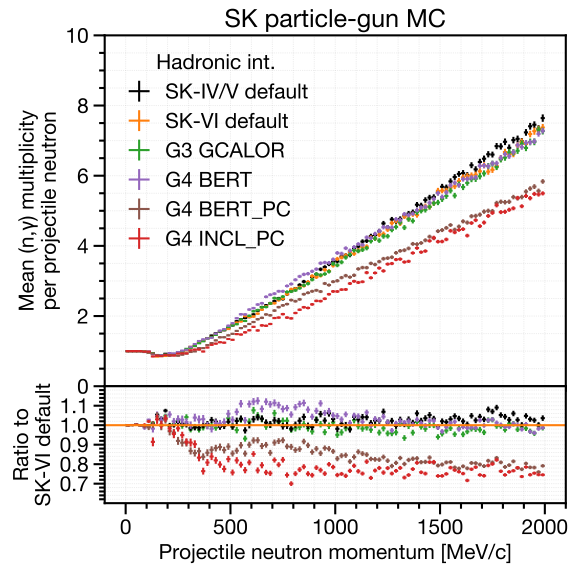


FIG. 14. Comparison of secondary hadron-nucleus interaction models: Average  $(n, \gamma)$  multiplicity per projectile neutron momentum bin, based on simulations using a single-neutron particle-gun setup in water.

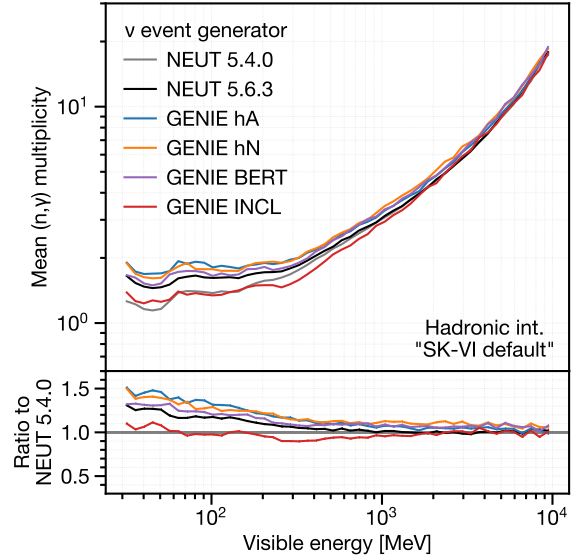


FIG. 15. Comparison of the predicted average  $(n, \gamma)$  multiplicity predicted by the neutrino event generator options paired with **SK-VI default**.

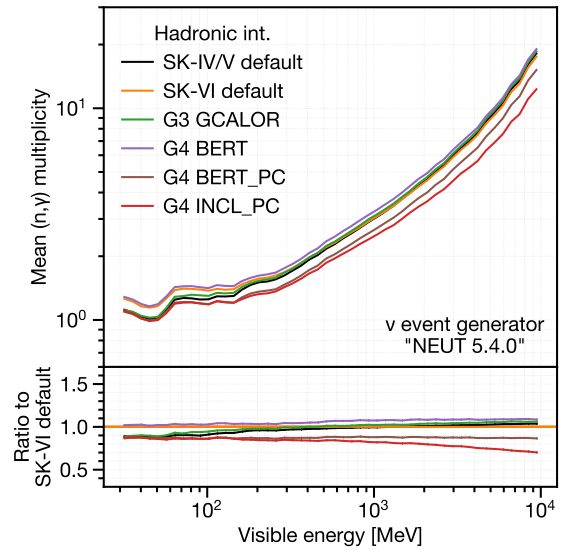


FIG. 16. Comparison of the predicted average  $(n, \gamma)$  multiplicity predicted by the secondary hadron-nucleus interaction models paired with **NEUT 5.4.0**.

Figure 13 compares outgoing neutron momentum distributions predicted by the six neutrino event generator options, highlighting notable differences below 1 GeV/c, which are further discussed in Section VIII. For each neutrino event generator, a full MC simulation equivalent to 50 years of atmospheric neutrino exposure was generated using the baseline detector model (**SK-VI default**). To account for variations in secondary hadron-nucleus interactions without additional full simulations, we precomputed average signal multiplicities for neutron-producing projectiles ( $n, p, \pi^\pm$ , and  $\mu^-$ ) in water up to 10 GeV/c, based on particle-gun MC simulations.

Figure 13 compares outgoing neutron momentum distributions predicted by the six neutrino event generator options, highlighting notable differences below 1 GeV/c, which are further discussed in Section VIII.

Figure 14 shows the average signal multiplicities as a function of projectile neutron momentum for the six secondary hadron-nucleus interaction models, with variations of up to 40%.

Predictions were made by convolving hadron momentum distributions with momentum-to-multiplicity tables. For each event generator, ratios relative to the baseline detector simulation model (**SK-VI default**) were used to scale the signal multiplicities obtained from the full MC simulation. In configurations using either **NEUT 5.4.0** or **NEUT 5.6.3** with **SK-IV/V default**, the discrepancy between this prediction method and the 500-year exposure full MC simulation was within 5% across all visible energy range and data subsamples.

Figures 15 and 16 show the model predictions. In visible energy range above a few hundred MeV, the average  $(n, \gamma)$  multiplicities are expected to increase linearly with visible energy. Differences across neutrino event generator configurations are more pronounced at visible energies below 1 GeV, while variability among secondary hadron-nucleus interaction models remains relatively constant. **GENIE INCL** predicts fewer neutrons than the other FSI models, as already suggested by Figure 13. **NEUT 5.4.0** predicts fewer neutrons than **NEUT 5.6.3**, due to a larger QE fraction. Additionally, the **Geant4 Bertini cascade model with the Precompound model (G4 BERT\_PC)** predicts fewer neutrons than when using the native de-excitation model (**G4 BERT**).

## VII. RESULTS

Table III summarizes the number of atmospheric neutrino events and detected neutron signals in the final data sample. The overall average  $(n, \gamma)$  multiplicity per neutrino event,  $\langle N \rangle_{\text{overall}}$ , is estimated using Equation 4 for all selected atmospheric neutrino events without binning.

The combined data was compared with the baseline simulation and neutron production estimates in water from SNO [14], as shown in Figure 17. For visible energies above 200 MeV—where outgoing lepton Cherenkov rings are well reconstructed—a linear relationship between visible energy and the average  $(n, \gamma)$  multiplicity was observed, as expected. While the data aligned well with the SNO estimate, it was 10–30% lower than the baseline predictions in the sub-GeV energy range. A similar deficit was reported by SNO in heavy water [14], where their data was compared to **GENIE 2.10.2 (hA FSI model)** coupled with the **Geant4 Bertini cascade model**.

Predictions from various model combinations, as described in Section VI, were compared with the combined data across different subsamples, as shown in Figure 18. The bottom panel of Figure 18 contrasts the data with predictions from selected FSI models (**GENIE hN** and **INCL**) and secondary interaction models (**G4 BERT**, **G4 BERT\_PC**, and **G4 INCL\_PC**). The observed deficit in the [0.1, 0.4] GeV range was primarily found in the single-ring sample, which is expected to be dominated by CCQE interactions (see Figure 5). This deficit was only reproduced when using models that predict fewer neutrons than the baseline for both FSI and secondary interactions, such as **GENIE INCL** and **G4 BERT\_PC**.

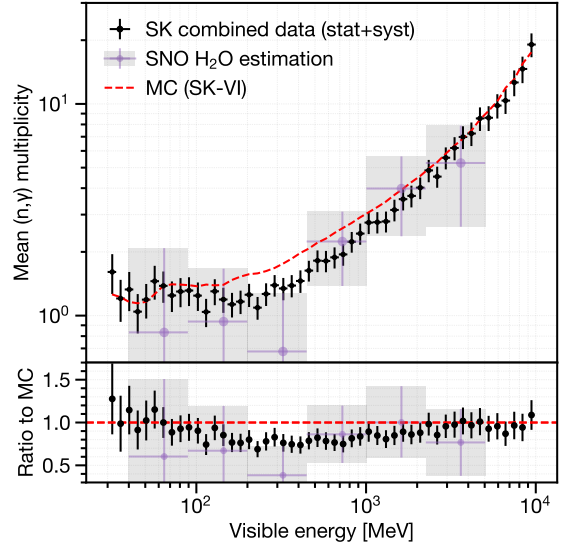


FIG. 17. Average  $(n, \gamma)$  multiplicity in atmospheric neutrino events as a function of their visible energy. Black data points represent combined SK data with statistical and systematic uncertainties. Purple crosses with shades are estimates for pure water based on SNO measurements [14] using a D<sub>2</sub>O target. The red dashed line represents the true average  $(n, \gamma)$  multiplicity from the baseline SK-IV MC simulation.

In the multi-ring sample at a few-GeV energies, there was significant variation in the predicted “slope” of the average  $(n, \gamma)$  multiplicity as a function of visible energy. In particular, **G4 INCL\_PC** predicted a smaller slope compared to **G4 BERT** and **G4 BERT\_PC**.

The goodness of fit between model predictions and data for the entire visible energy range of [0.03, 10] GeV was quantified using the following chi-square ( $\chi^2$ ) definition, considering only the two most dominant sources of uncertainty: statistical uncertainty and signal efficiency scale uncertainty.

$$\chi^2 = \sum_i^{N_{\text{bins}}} \frac{(sO_i - E_i)^2}{\sigma_{\text{stat},i}^2} \quad (5)$$

Here,  $i$  is the bin number,  $O_i$  and  $E_i$  represent the observed and expected average  $(n, \gamma)$  multiplicity, respectively, and  $\sigma_{\text{stat},i}$  is the statistical uncertainty in the  $i$ -th bin. The total number of bins,  $N_{\text{bins}}$ , is 20 per subsample for both single-ring and multi-ring events, resulting in 40 bins in total. The binning was optimized to ensure a sufficient number of events per bin so that the average  $(n, \gamma)$  multiplicity follows a normal distribution. The normalization scale  $s$  was allowed to float within [0, 2]. Two  $\chi^2$  calculations were performed: (1) a normalization-free  $\chi^2$ , where  $s$  was minimized without constraint, and (2) a constrained  $\chi^2$ , where  $s$  was minimized with a penalty term  $(s-1)^2/\sigma_{\text{scale}}^2$  and an additional constraint  $|s-1| < \sigma_{\text{scale}}$ , with  $\sigma_{\text{scale}}$  set to 10%.

TABLE III. A summary of the number of atmospheric neutrino events (“ $\nu$  events”) and detected neutron signals (“ $n$  signals”) in the final sample.  $\langle N \rangle_{\text{overall}}$  is the unbinned application of Equation 4, followed by signal efficiency scale corrections with the factors given in Section IV B. These factors are specifically chosen to ensure consistency of  $\langle N \rangle_{\text{overall}}$  across the three SK phases (see Appendix A). Errors for the observed  $\langle N \rangle_{\text{overall}}$  are listed as statistical first, followed by systematic uncertainty. Other errors are statistical only. The bottom two rows show the expected  $\langle N \rangle_{\text{overall}}$  and the true overall  $(n, \gamma)$  multiplicity extracted from the baseline full MC simulations (NEUT 5.4.0 with **SK-IV/V default** for SK-IV/V, and **SK-VI default** for SK-VI).

	SK-IV	SK-V	SK-VI
$\nu$ events	29,942	4,231	5,203
Events/day	$9.23 \pm 0.05$	$9.18 \pm 0.14$	$9.22 \pm 0.13$
$n$ signals	15,705	2,035	5,752
$n$ signals/event	$0.525 \pm 0.004$	$0.481 \pm 0.011$	$1.106 \pm 0.015$
Observed $\langle N \rangle_{\text{overall}}$	$2.49 \pm 0.03 \pm 0.23$	$2.49 \pm 0.10 \pm 0.11$	$2.49 \pm 0.06 \pm 0.05$
Expected $\langle N \rangle_{\text{overall}}$	2.83	2.84	2.85
True $(n, \gamma)$ multiplicity	2.85	2.85	2.86

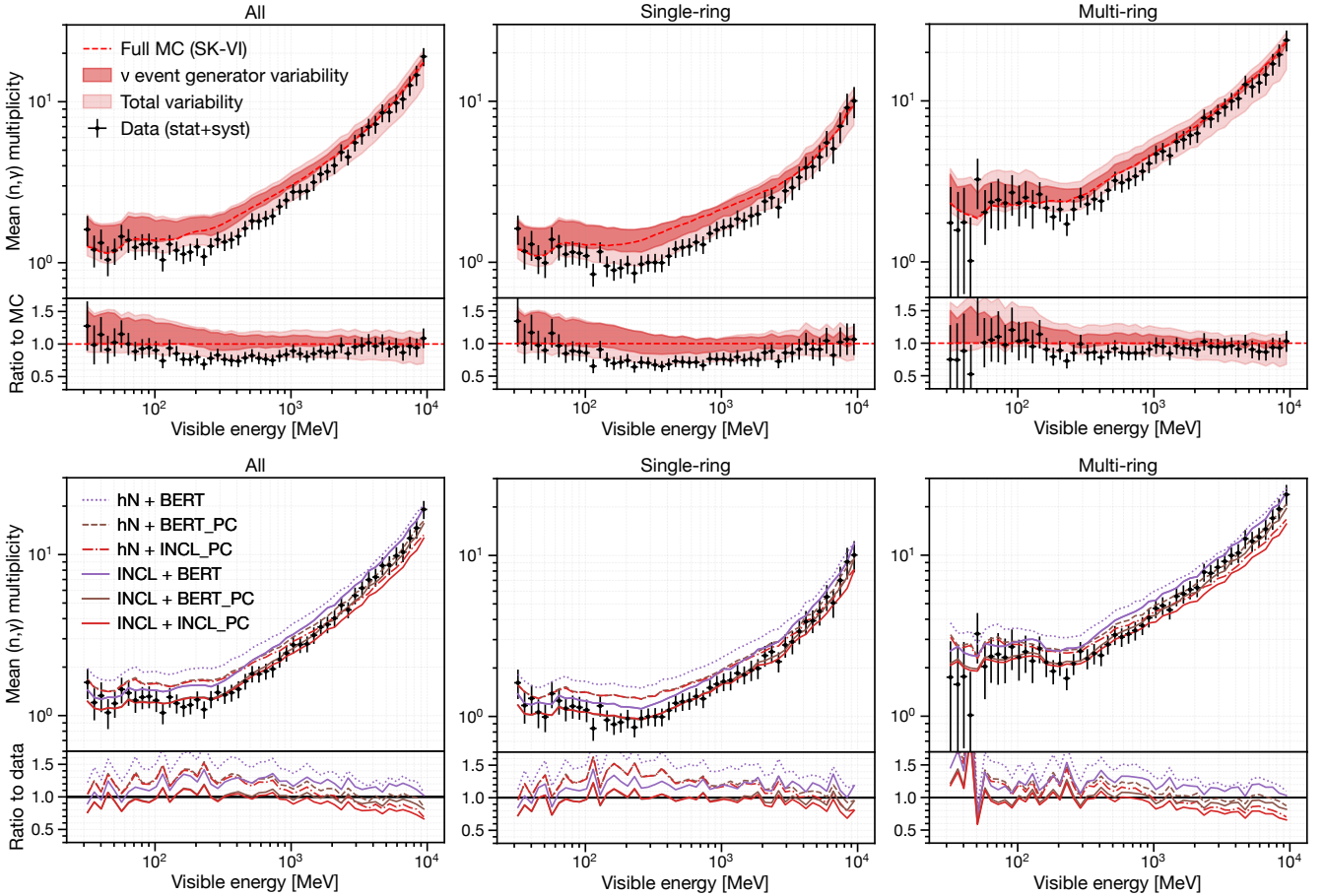


FIG. 18. Comparison of various model predictions with the combined data, showing the average  $(n, \gamma)$  multiplicity as a function of atmospheric neutrino event visible energy, for all events (left), single-ring events (middle), and multi-ring events (right). The black data points represent the combined data, including both statistical and systematic uncertainties. In the top panel, the combined data are compared to the prediction intervals of the models. Thicker shaded regions represent the range of predictions obtained by varying only the neutrino event generator options while keeping the secondary hadron-nucleus interaction model fixed to the baseline (**SK-VI default**). Lighter shaded regions indicate the broader range of predictions from all model combinations. The bottom panel shows corresponding plots for specific model choices that are based on GENIE and Geant4, including the one (**GENIE INCL + G4 BERT\_PC**) that shows good agreement with the data (see Table IV).

TABLE IV. Reduced  $\chi^2$  (see Equation 5) and  $p$ -values for each model combination. The signal efficiency scale  $s$  was either freely minimized or constrained to 10%. The fit has 38 fixed degrees of freedom.  $p$ -values assume Gaussian bin errors without bin correlations.

$\nu$ generator	Secondary int.	Minimizing $s$		Reduced $\chi^2$		$p$ -value	
		Free $s$	Constrained $s$	Free $s$	Constrained $s$	Free $s$	Constrained $s$
1	NEUT 5.4.0	SK-IV/V default	0.75	0.90	2.76	11.66	$< 10^{-4}$
2	NEUT 5.4.0	SK-VI default	0.74	0.90	3.64	14.38	$< 10^{-4}$
3	NEUT 5.4.0	G3 GCALOR	0.73	0.90	2.14	13.47	$< 10^{-4}$
4	NEUT 5.4.0	G4 BERT	0.70	0.90	2.14	20.76	$< 10^{-4}$
5	NEUT 5.4.0	G4 BERT_PC	0.84	0.90	2.73	3.68	$< 10^{-4}$
6	NEUT 5.4.0	G4 INCL_PC	0.89	0.90	5.08	5.11	$< 10^{-4}$
7	NEUT 5.6.3	SK-IV/V default	0.72	0.90	2.92	15.94	$< 10^{-4}$
8	NEUT 5.6.3	SK-VI default	0.71	0.90	4.40	19.97	$< 10^{-4}$
9	NEUT 5.6.3	G3 GCALOR	0.71	0.90	2.24	18.30	$< 10^{-4}$
10	NEUT 5.6.3	G4 BERT	0.67	0.90	2.53	27.88	$< 10^{-4}$
11	NEUT 5.6.3	G4 BERT_PC	0.81	0.90	3.38	5.87	$< 10^{-4}$
12	NEUT 5.6.3	G4 INCL_PC	0.86	0.90	6.38	6.86	$< 10^{-4}$
13	GENIE hA	SK-IV/V default	0.73	0.90	3.17	14.83	$< 10^{-4}$
14	GENIE hA	SK-VI default	0.67	0.90	6.71	30.43	$< 10^{-4}$
15	GENIE hA	G3 GCALOR	0.71	0.90	2.47	17.69	$< 10^{-4}$
16	GENIE hA	G4 BERT	0.65	0.90	3.73	36.46	$< 10^{-4}$
17	GENIE hA	G4 BERT_PC	0.77	0.90	5.29	10.91	$< 10^{-4}$
18	GENIE hA	G4 INCL_PC	0.80	0.90	9.64	12.93	$< 10^{-4}$
19	GENIE hN	SK-IV/V default	0.71	0.90	1.75	16.50	0.0030
20	GENIE hN	SK-VI default	0.66	0.90	4.32	31.29	$< 10^{-4}$
21	GENIE hN	G3 GCALOR	0.69	0.90	1.48	20.77	0.028
22	GENIE hN	G4 BERT	0.63	0.90	2.29	40.19	$< 10^{-4}$
23	GENIE hN	G4 BERT_PC	0.76	0.90	3.13	10.10	$< 10^{-4}$
24	GENIE hN	G4 INCL_PC	0.79	0.90	6.48	10.34	$< 10^{-4}$
25	GENIE BERT	SK-IV/V default	0.75	0.90	1.22	9.79	0.17
26	GENIE BERT	SK-VI default	0.70	0.90	3.31	21.35	$< 10^{-4}$
27	GENIE BERT	G3 GCALOR	0.73	0.90	1.21	13.69	0.17
28	GENIE BERT	G4 BERT	0.67	0.90	1.79	27.70	0.0020
29	GENIE BERT	G4 BERT_PC	0.80	0.90	2.56	6.06	$< 10^{-4}$
30	GENIE BERT	G4 INCL_PC	0.83	0.90	5.60	7.12	$< 10^{-4}$
31	GENIE INCL	SK-IV/V default	0.87	0.90	0.84	1.21	0.74
32	GENIE INCL	SK-VI default	0.80	0.90	1.33	4.59	0.082
33	GENIE INCL	G3 GCALOR	0.83	0.90	1.36	2.75	0.067
34	GENIE INCL	G4 BERT	0.76	0.90	0.87	8.55	0.71
35	GENIE INCL	G4 BERT_PC	0.92	0.92	0.95	0.96	0.56
36	GENIE INCL	G4 INCL_PC	0.97	0.97	2.74	2.74	$< 10^{-4}$

Table IV compares the reduced  $\chi^2$  values across different model combinations. Among the neutrino event generator options, GENIE INCL showed the lowest  $\chi^2$  for both free and constrained  $s$ . Among the secondary interaction models, G4 BERT\_PC provided the best agreement with data under the 10% normalization constraint. The combination of these two models yielded the best overall agreement under the same constraint. Other secondary interaction models such as SK-IV/V default showed reasonable agreement when coupled with GENIE INCL or when normalization was allowed to float. In contrast, G4 INCL\_PC showed higher unconstrained  $\chi^2$  values, due to the shallower slope prediction for the multi-ring events.

Model performance, separated into contributions from target nucleus FSI and secondary interactions, is further

visualized using effective metrics in Appendix B.

## VIII. DISCUSSION

Overall, our data favor models that predict relatively lower neutron production for single-ring sub-GeV events and higher neutron production for multi-ring multi-GeV events. In this section, we examine key features of these models that influence neutron production predictions, focusing on Figure 13, which illustrates differences in neutron momentum distributions across the tested FSI models. By qualitatively comparing the features of these models, we discuss potential factors contributing to the observed discrepancies in predictions.

### 809 A. Nuclear de-excitation

863      **A. Nuclear de-excitation**

810      Nuclear de-excitation models are crucial for predict-<sup>863</sup>  
 811      ing total neutron production, as they govern low-energy<sup>866</sup>  
 812      neutron emission per nuclear interaction. This is evident<sup>867</sup>  
 813      when comparing G4 BERT and G4 BERT\_PC, which differ<sup>868</sup>  
 814      only in their de-excitation treatment. For instance, the<sup>869</sup>  
 815      inaccuracy of the Geant4 Bertini cascade model predi-<sup>870</sup>  
 816      cation is indicated by the distinct large neutron peak be-<sup>871</sup>  
 817      low 250 MeV/c in GENIE BERT (Figure 13), compared to<sup>872</sup>  
 818      the other models such as ABLA07 in GENIE INCL or the<sup>873</sup>  
 819      native de-excitation model in NEUT. (The GENIE hA and<sup>874</sup>  
 820      hN options omit nuclear de-excitation entirely.) Coupling<sup>875</sup>  
 821      the Geant4 Precompound model with the Geant4 Bertini<sup>876</sup>  
 822      cascade model significantly reduces neutron production<sup>877</sup>  
 823      across all visible energy ranges, leading to much better<sup>878</sup>  
 824      agreement with data (Figure 18).

825      In the Geant4 Bertini cascade model, neutron emis-<sup>826</sup>  
 826      sion follows the Weisskopf statistical evaporation model<sup>827</sup>  
 827      [62]. A key input determining neutron emission proba-<sup>828</sup>  
 828      bility is the inverse reaction (neutron absorption) cross<sup>829</sup>  
 829      section. The inaccuracy of the Bertini model and its vari-<sup>830</sup>  
 830      ants in predicting neutron evaporation may stem from<sup>831</sup>  
 831      its use of the simplified cross section parameterization<sup>832</sup>  
 832      by Dostrovsky [63]. In comparison, the Geant4 Precom-<sup>833</sup>  
 833      pound model uses a more refined parameterization based<sup>834</sup>  
 834      on the nuclear optical model potential [64], fitted to a<sup>835</sup>  
 835      broader dataset [65], resulting in lower evaporation rates<sup>836</sup>  
 836      particularly for low-energy neutrons. Additionally, the<sup>837</sup>  
 837      Geant4 Precompound model features tuned level den-<sup>838</sup>  
 838      sity parameters and allows Fermi breakup in nuclei up<sup>839</sup>  
 839      to mass 16 [60], including oxygen, further reducing iso-<sup>840</sup>  
 840      lated neutrons that contribute to  $(n, \gamma)$  signals.

### 841 B. Nuclear in-medium effects

894      **B. Nuclear in-medium effects**

842      A key distinction among the FSI cascade models is<sup>896</sup>  
 843      their treatment of Pauli blocking, which prevents nu-<sup>897</sup>  
 844      cleons from occupying the same quantum state, as dic-<sup>898</sup>  
 845      cated by the Pauli exclusion principle. For instance, NEUT<sup>899</sup>  
 846      5.4.0, NEUT 5.6.3 and GENIE BERT implement “strict”<sup>900</sup>  
 847      Pauli blocking, which forbids all nucleon scattering be-<sup>901</sup>  
 848      low the predefined oxygen Fermi momentum around 225  
 849      MeV/c, modeling the nucleus as a degenerate Fermi gas.<sup>902</sup>  
 850      This approach results in a characteristic dip in the out-<sup>903</sup>  
 851      going neutron momentum distributions for NEUT 5.4.0  
 852      and NEUT 5.6.3 within the corresponding energy range,<sup>904</sup>  
 853      as shown in Figure 13. The Liège INC model applies<sup>905</sup>  
 854      a probabilistic approach for nucleon collisions throughout<sup>906</sup>  
 855      the cascade (except for the initial collision), accounting<sup>907</sup>  
 856      for nucleon holes in the surrounding phase space volume<sup>908</sup>  
 857      [66, 67]. This results in smoother neutron distributions<sup>909</sup>  
 858      near the Fermi momentum, as seen in Figure 13. In con-<sup>910</sup>  
 859      trast, the GENIE hA and hN models omit Pauli blocking<sup>911</sup>  
 860      entirely, leading to significantly higher predicted neutron<sup>912</sup>  
 861      production than NEUT 5.4.0, NEUT 5.6.3, and GENIE<sup>913</sup>  
 862      INCL.

863      In the 0.2–1GeV/c range, the number of outgoing neu-  
 864      trons predicted by the Liège INC and Geant4 Bertini cas-  
 865      cade models is lower than that from the GENIE hA, hN,  
 866      and NEUT nucleon FSI models, as illustrated in Figure 13.  
 867      One contributing factor may be the inclusion of light  
 868      cluster formation—such as deuterons, tritons, and alpha  
 869      particles—among cascade products, which reduces the  
 870      number of isolated neutrons contributing to the observ-  
 871      able signal. Ref. [68] also identifies cluster formation as a  
 872      major mechanism behind the reduction of outgoing pro-  
 873      tons in the Liège INC model. Additional in-medium ef-  
 874      fects, considered either explicitly or implicitly in the two  
 875      models—such as short-range nucleon repulsion and local  
 876      nuclear density reduction after each collision—further re-  
 877      duce the number of nucleon-nucleon collisions during the  
 878      cascade.

### 879 C. $\pi^\pm$ production

880      **C.  $\pi^\pm$  production**

881      Accurate modeling of pion-nucleus interactions is cru-  
 882      cial for predicting neutron production in multi-ring  
 883      events with energetic pions (see Figures 24 and 25 in Ap-  
 884      pendix C). The difference in predicted neutron produc-  
 885      tion in the few-GeV multi-ring sample between the Liège  
 886      INC model (G4 INCL\_PC) and the Geant4 Bertini cascade  
 887      model (G4 BERT\_PC), as observed in Figure 18, can be at-  
 888      tributed to differences in pion production cross sections  
 889      for pion projectiles. Our results are consistent with those  
 890      of Ref. [69], which report that the Liège INC model tends  
 891      to predict lower inclusive  $\pi^\pm$  production cross sections  
 892      on light nuclei (mass number  $A < 20$ ) compared to the  
 893      Geant4 Bertini cascade model. In addition, the pion po-  
 894      tential within the nucleus differs between the two models.  
 895      In the Liège INC model, the pion potential is generally  
 896      deeper [70] than the constant 7 MeV potential used in the  
 897      Geant4 Bertini cascade model [57], which impacts pion  
 898      transparency. For instance, Ref. [71] demonstrated that  
 899      the Liège INC model shows lower pion transparency for  
 900      pions with momenta below 300 MeV/c compared to the  
 901      GENIE hA, hN, or NEUT pion FSI models.

### 902 D. Other considerations

903      **D. Other considerations**

904      Variations in low-energy neutron reaction cross section  
 905      datasets (e.g., ENDF/B-VI used in SK-IV/V default vs.  
 906      ENDF/B-VII.1 used in SK-VI default) result in a 5–  
 907      10% difference in the average  $(n, \gamma)$  multiplicities for vis-  
 908      ible energy below 300 MeV, as shown in Figure 16. Our  
 909      model predictions do not account for interactions of  $\nu_\tau$   
 910      and  $\bar{\nu}_\tau$  from oscillations, nor neutrinos with energies be-  
 911      low 100 MeV. However, their contributions are expected  
 912      to be smaller than our uncertainty budget in the upper  
 913      and lower ends of the visible energy range, where their  
 914      effects become relevant, respectively.

913

## IX. CONCLUSIONS AND PROSPECTS

965

## ACKNOWLEDGMENTS

914 Accurately modeling neutron production in neutrino<sup>967</sup>  
 915 interactions is essential for characterizing incoming neu-<sup>968</sup>  
 916 trinos, which is crucial for advancing precision measure-<sup>969</sup>  
 917 ments of neutrino oscillation parameters and rare event<sup>970</sup>  
 918 searches involving neutron tagging. Recent studies have<sup>971</sup>  
 919 suggested potential inaccuracies in the modeling of sec-<sup>972</sup>  
 920 ondary hadron-nucleus interactions.<sup>973</sup>

921 This paper reports a measurement of total neutron<sup>974</sup>  
 922 production following atmospheric neutrino interactions<sup>975</sup>  
 923 within the water volume of the Super-Kamiokande (SK)<sup>976</sup>  
 924 detector. Atmospheric neutrino events were binned<sup>977</sup>  
 925 by their electron-equivalent “visible energy,” a semi-<sup>978</sup>  
 926 calorimetric proxy for neutrino momentum transfer, in<sup>979</sup>  
 927 the range of [0.03, 10] GeV. The dominant systematic<sup>980</sup>  
 928 uncertainty was the roughly 10% uncertainty in the over-<sup>981</sup>  
 929 all signal efficiency scale. The average neutron cap-<sup>982</sup>  
 930 ture multiplicity in each visible energy bin was compared<sup>983</sup>  
 931 against predictions from various combinations of neutrino<sup>984</sup>  
 932 event generators and secondary hadron-nucleus interac-<sup>985</sup>  
 933 tion models.<sup>986</sup>

934 Our data provides strong discriminative power for eval-<sup>987</sup>  
 935 uating these models, with predictions varying by up to<sup>988</sup>  
 936 50%. Two key observations were made: a reduction in<sup>989</sup>  
 937 neutron production for sub-GeV single-ring events, where<sup>990</sup>  
 938 secondary hadron interactions are minimal, and a nearly<sup>991</sup>  
 939 linear increase in neutron production with visible energy,<sup>992</sup>  
 940 especially in the multi-GeV region. The first observa-<sup>993</sup>  
 941 tion highlights the need for moderate neutron evapora-<sup>994</sup>  
 942 tion and consideration of nuclear in-medium effects. The<sup>995</sup>  
 943 second is more sensitive to pion production in cascade<sup>996</sup>  
 944 models, which become important at higher energies.<sup>997</sup>

945 This study highlights the crucial role of hadron-nucleus<sup>1000</sup>  
 946 interaction models in accurately predicting total neutron  
 947 production from neutrino interactions. The observed<sup>1001</sup>  
 948 discrepancy with the evaporation model [63] commonly<sup>1002</sup>  
 949 used in Bertini-based cascade models aligns with previ-<sup>1003</sup>  
 950 ous studies, including neutron measurements with NCQE<sup>1004</sup>  
 951 selections [17] at SK and secondary  $\gamma$ -ray measurements<sup>1005</sup>  
 952 using Germanium detectors with a neutron beam on a<sup>1006</sup>  
 953 water target [72–74]. Our data also supports the selec-<sup>1007</sup>  
 954 tion of specific models, such as GENIE INCL and G4<sup>1008</sup>  
 955 BERT\_PC, which reduce the uncertainty in total neutron<sup>1009</sup>  
 956 production from atmospheric neutrino events to around<sup>1010</sup>  
 957 10%. These models may help explain the deficits in total<sup>1011</sup>  
 958 neutron capture signals reported by T2K [13] and SNO<sup>1012</sup>  
 959 [14], and offer insights into the low-energy neutron signal<sup>1013</sup>  
 960 deficits observed in MINERvA [2]. Lastly, this work will<sup>1014</sup>  
 961 improve the use of neutron tagging for identifying atmo-<sup>1015</sup>  
 962 spheric antineutrino events at SK, enhancing sensitivity<sup>1016</sup>  
 963 to neutrino mass ordering and searches for proton decay<sup>1017</sup>  
 964 and the diffuse supernova neutrino background.<sup>1018</sup>

966 We gratefully acknowledge the cooperation of the  
 Kamioka Mining and Smelting Company. The Super-  
 Kamiokande experiment has been built and operated  
 from funding by the Japanese Ministry of Education,  
 Culture, Sports, Science and Technology; the U.S.  
 Department of Energy; and the U.S. National Sci-  
 ence Foundation. Some of us have been supported  
 by funds from the National Research Foundation of  
 Korea (NRF-2009-0083526, NRF-2022R1A5A1030700,  
 NRF-2202R1A3B1078756) funded by the Ministry of  
 Science, Information and Communication Technology  
 (ICT); the Institute for Basic Science (IBS-R016-Y2);  
 and the Ministry of Education (2018R1D1A1B07049158,  
 2021R1I1A1A01042256, 2021R1I1A1A01059559, RS-  
 2024-00442775); the Japan Society for the Promotion  
 of Science; the National Natural Science Foundation of  
 China under Grants No.12375100; the Spanish Ministry  
 of Science, Universities and Innovation (grant PID2021-  
 124050NB-C31); the Natural Sciences and Engineer-  
 ing Research Council (NSERC) of Canada; the Scinet  
 and Westgrid consortia of Compute Canada; the Na-  
 tional Science Centre (UMO-2018/30/E/ST2/00441 and  
 UMO-2022/46/E/ST2/00336) and the Ministry of Sci-  
 ence and Higher Education (2023/WK/04), Poland;  
 the Science and Technology Facilities Council (STFC)  
 and Grid for Particle Physics (GridPP), UK; the Eu-  
 ropean Union’s Horizon 2020 Research and Innova-  
 tion Programme under the Marie Skłodowska-Curie  
 grant agreement no.754496; H2020-MSCA-RISE-2018  
 JENNIFER2 grant agreement no.822070, H2020-MSCA-  
 RISE-2019 SK2HK grant agreement no. 872549; and  
 European Union’s Next Generation EU/PRTR grant  
 CA3/RSUE2021-00559; the National Institute for Nu-  
 clear Physics (INFN), Italy.

### Appendix A: $\langle N \rangle_{\text{overall}}$ consistency across SK phases

When applying a signal efficiency correction based on the weighted mean of Am/Be data-to-MC efficiency ratios—as shown in Figure 10 and described in Section IV B—the efficiency-corrected estimate of total neutron production  $\langle N \rangle_{\text{overall}}$  was  $2.21 \pm 0.03 \text{ (stat)} \pm 0.11 \text{ (syst)}$  in SK-IV, lower than the values observed in the other two phases:  $2.46 \pm 0.10 \pm 0.11$  for SK-V and  $2.50 \pm 0.06 \pm 0.05$  for SK-VI. This discrepancy may be due to unaccounted systematic uncertainties in SK-IV, which had the longest data-taking period (nearly 10 years) but only a limited amount of calibration data to constrain the entire duration. In contrast, SK-VI—with a much shorter runtime (about 2 years)—periodically took calibration data across various positions within the detector volume. Thus, the signal efficiency scale for SK-VI is considered more reliable than that of SK-IV.

To test the robustness of the signal efficiency correction derived from the Am/Be calibration data and simulation,

we applied an alternative neutron signal detection algorithm to both the calibration and atmospheric neutrino datasets in SK-VI. This algorithm uses a likelihood-based vertex fitter [75] to reconstruct the  $Gd(n, \gamma)$  vertex independently of the neutrino interaction vertex, making it more resilient to uncertainties in outgoing neutron kinematics that affect the detection efficiency in the baseline algorithm described in Section IV A. Using this reference algorithm, we obtained  $\langle N \rangle_{\text{overall}} = 2.49 \pm 0.06 \pm 0.05$  for SK-VI, consistent with the baseline result.

Relying on the signal efficiency scale obtained for SK-VI, we adjust the correction factors for all phases such that  $\langle N \rangle_{\text{overall}}$  aligns with the SK-VI reference value of 2.49. The difference between the calibration-based and phase-consistency-based correction factors is treated as an independent systematic uncertainty in the signal efficiency scale and is included in the uncertainty budget shown in Figure 12. This yields a final  $\langle N \rangle_{\text{overall}}$  of  $2.49 \pm 0.03 \text{ (stat)} \pm 0.26 \text{ (syst)}$ , corresponding to a total systematic uncertainty of approximately 10%. Figure 19 illustrates the impact of the two signal efficiency correction approaches: one based on Am/Be neutron source calibration and the other based on phase consistency.

## Appendix B: Effective metrics for model evaluation

To separately evaluate the contributions from FSI within the target nucleus and downstream secondary interactions, we define two effective metrics. The first metric is the low-energy (low-E) multiplicity as the average  $(n, \gamma)$  multiplicity in the  $[0.1, 0.3]$  GeV visible energy range, where the contribution of low-energy nucleon FSI is significant (see Figure 23 in Appendix C). Events below 0.1 GeV are excluded due to large systematic uncertainties. The second metric is the slope of the linear increase in average  $(n, \gamma)$  multiplicity as a function of visible energy, obtained by performing a linear fit over the range  $[0.3, 10]$  GeV, as shown in Figure 20.

Figure 21 compares the measured slopes and low-energy multiplicities across different SK phases and event topologies. For the slope fits shown in the figure, the binning scheme was adjusted to ensure sufficient statistics (typically  $\gtrsim 30$  neutrino events per bin). The measured values are consistent across SK phases within the assigned uncertainties. Both metrics are higher for multi-ring events than for single-ring events, as expected due to the higher fraction of deep inelastic scattering (DIS) interactions in the multi-ring sample (see Figure 5). While the observed slopes agree with baseline model predictions, the measured low-energy multiplicities were lower than expected.

Figure 22 compares the measured slopes and low-energy multiplicities with model predictions. The predictions show three distinct groups of slopes: the G4 INCL\\_PC model gives the smallest slopes, G4 BERT\\_PC predicts intermediate slopes, and other variants of the Bertini cascade model produce the largest slopes. The

slope observed in the single-ring data better matches the G4 INCL\\_PC predictions, while the slope in the multi-ring data is closer to the G4 BERT\\_PC predictions. This distinction is most evident in the bottom panel of Figure 18, where G4 INCL\\_PC matches well with sub-GeV single-ring data, and G4 BERT\\_PC is a better fit for multi-GeV multi-ring data. For low-energy multiplicities, NEUT 5.4.0, NEUT 5.6.3, and GENIE INCL are preferred, as they predict lower neutron production. In contrast, models such as GENIE hA, hN, and BERT overestimate low-energy multiplicities, producing values significantly higher than the estimated  $1\sigma$  uncertainty. These trends in model predictions and agreement with data remained robust under variations in the visible energy ranges used to define both metrics.

## Appendix C: Sources of neutron production

Here, we clarify the sources of neutron production in our simulation. Figure 23 shows the baseline SK-IV neutron production as a function of visible energy. The number of outgoing neutrons from neutrino-nucleus interactions remains nearly constant across visible energies. At lower energies, the outgoing neutrons have small momenta, with each neutron corresponding closely to a single  $(n, \gamma)$  reaction. At higher energies, larger hadron momentum results in a linear increase in secondary neutron production. This indicates that, for the two metrics defined in Appendix B, the low-energy multiplicity is sensitive to nucleon transport modeling, while the slope is primarily determined by the secondary hadron-nucleus interaction model.

Figure 24 shows the contributions of nucleons and pions to the  $(n, \gamma)$  multiplicity as a function of visible energy, for different secondary hadron-nucleus interaction models. A general trend across all models is that, in the single-ring sample, most  $(n, \gamma)$  reactions are induced by outgoing nucleons from neutrino interactions, while in the multi-ring sample, outgoing pions dominate in the few-GeV range. Figure 25 further breaks down the contributions to the  $(n, \gamma)$  multiplicity by outgoing particle momentum, for two FSI models (GENIE INCL and GENIE hN) and two secondary interaction models (G4 INCL\\_PC and G4 BERT\\_PC). In single-ring atmospheric neutrino events with visible energy in the range  $[0.1, 0.3]$  GeV, the total  $(n, \gamma)$  multiplicity is primarily driven by neutrons below 1 GeV/c (from neutrino-nucleus interactions), with negligible variation across secondary interaction models. However, in multi-ring events with visible energies above 2 GeV, the total contribution from outgoing pions at all momenta becomes comparable to that from neutrons.

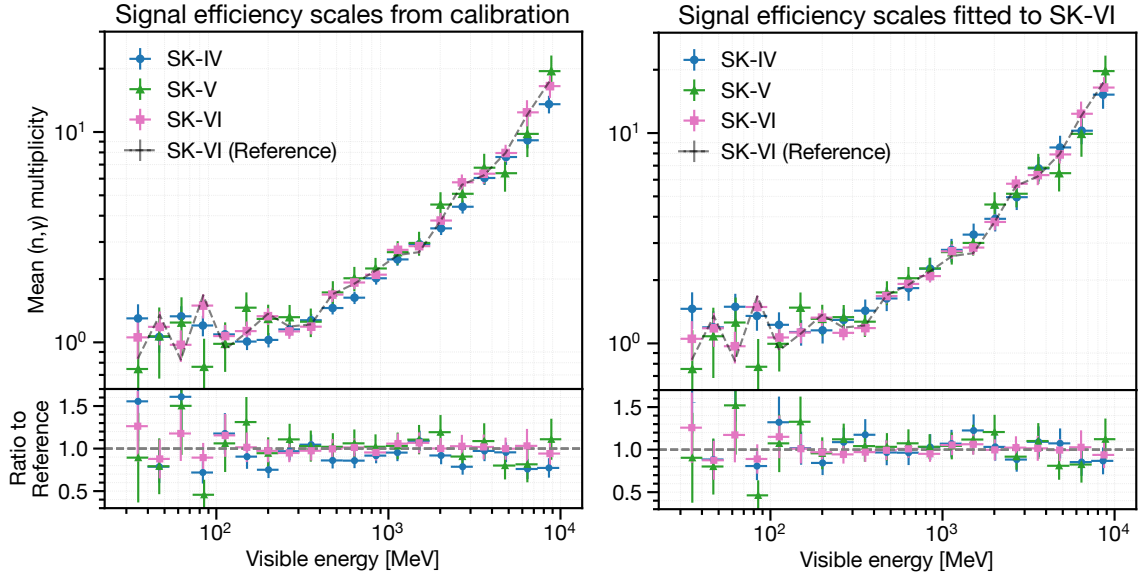


FIG. 19. Average  $(n, \gamma)$  multiplicities plotted against neutrino event visible energy across SK phases. The left plot uses signal efficiency scales from Am/Be calibration (Section IV B), while the right plot adjusts SK-IV and SK-V scales to match  $\langle N \rangle_{\text{total}}$  of SK-VI. Error bars include statistical and systematic uncertainties, with the right plot also accounting for scale differences. The dashed “SK-VI (Reference)” line shows SK-VI data using a neutron-energy-independent reference algorithm.

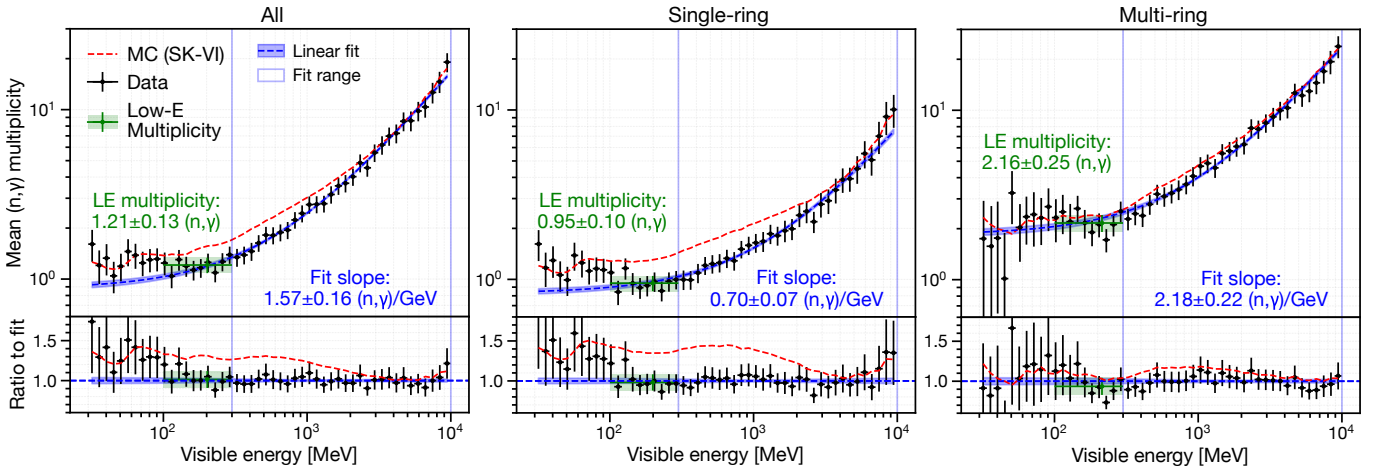


FIG. 20. Average  $(n, \gamma)$  multiplicity as a function of visible energy for neutrino events: all events (left), single-ring events (center), and multi-ring events (right). Red dashed lines show predictions from the full MC simulation in the SK-VI baseline setup. Blue dashed lines represent fitted linear functions with 1 $\sigma$  prediction intervals shaded in blue, with the fit covering the energy range [0.3, 10] GeV. Green points represent low-energy multiplicity in the [0.1, 0.3] GeV range. Error bars include both statistical and systematic uncertainties.

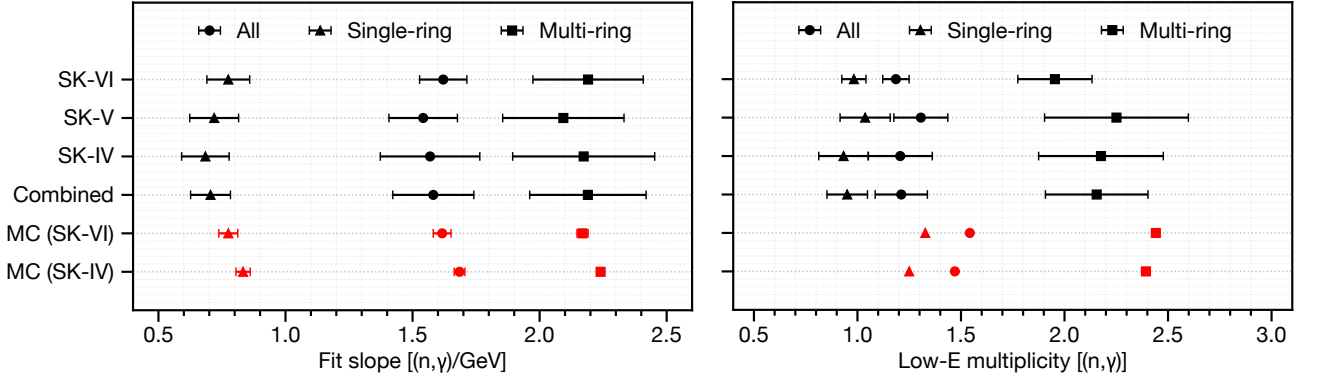


FIG. 21. Measured slopes (left) and low-energy multiplicities (right) across different SK phases and event types. Data error bars (black) represent both statistical and systematic uncertainties, while MC error bars in the left panel indicate statistical uncertainties. In the right panel, MC predictions correspond to the ‘true’ average  $(n, \gamma)$  multiplicity.

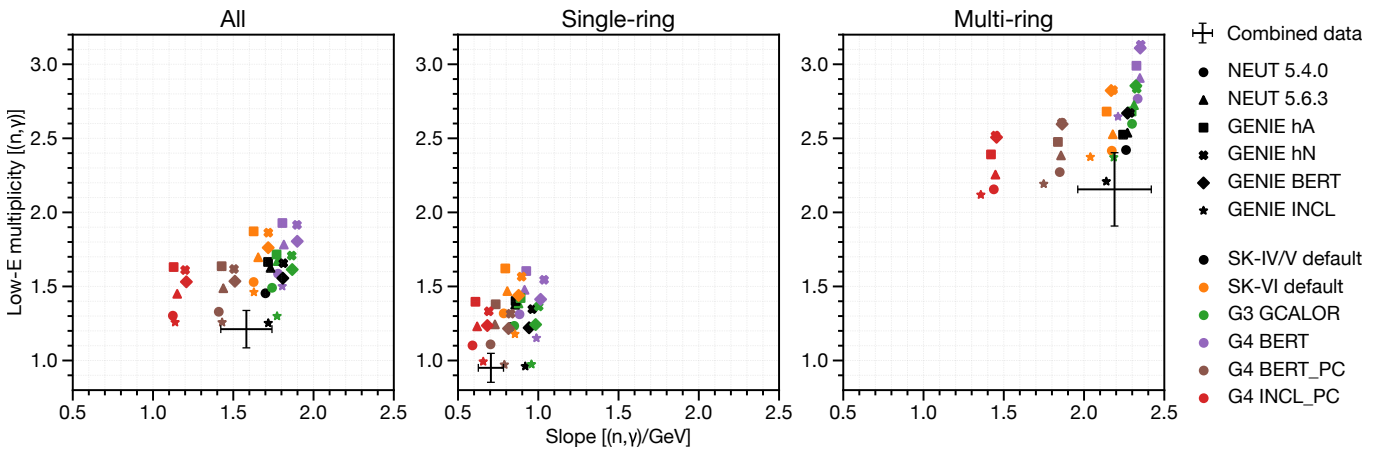


FIG. 22. Scatter plots of fitted slopes and low-energy multiplicities in model predictions and data (black crosses, error bars include both statistical and systematic uncertainties), shown for all events (left), single-ring events (middle), and multi-ring events (right). Shapes represent neutrino event generator options used, while colors indicate the secondary hadron-nucleus interaction model options used.

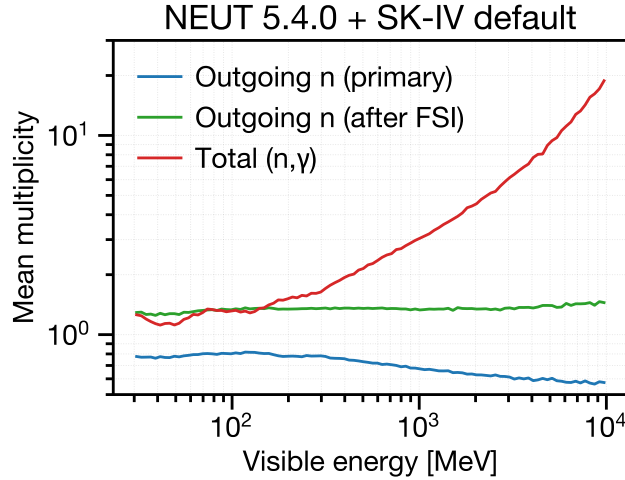


FIG. 23. Mean multiplicity of outgoing neutrons from the primary neutrino interaction (blue) and subsequent FSIs (green) and resulting total ( $n, \gamma$ ) reactions (red), in the baseline SK-IV simulation setup.

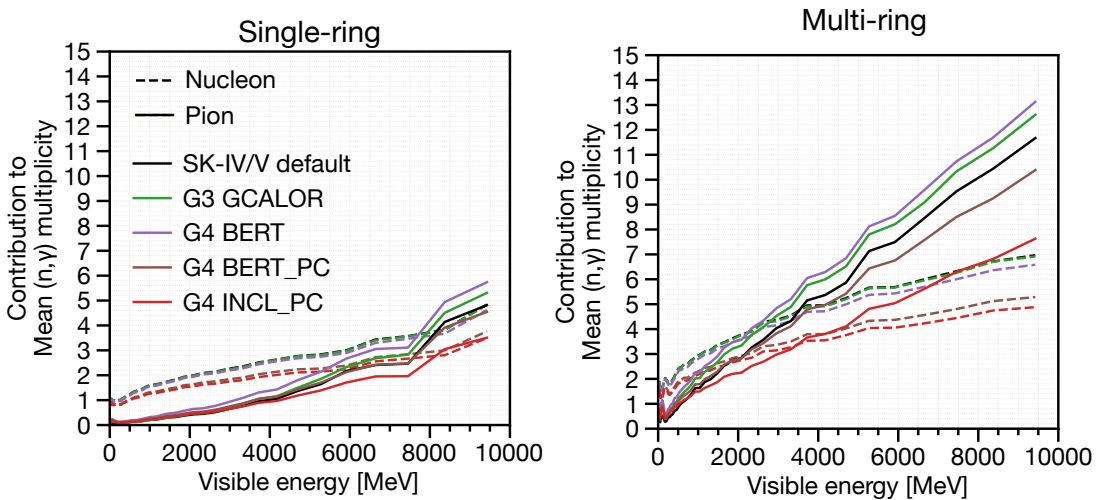


FIG. 24. Average contribution of outgoing nucleons (dashed lines) and pions (solid lines) to the observed ( $n, \gamma$ ) multiplicities as a function of visible energy, shown separately for single-ring events (top) and multi-ring events (bottom). The line colors represent different secondary hadron-nucleus interaction models used in the predictions.

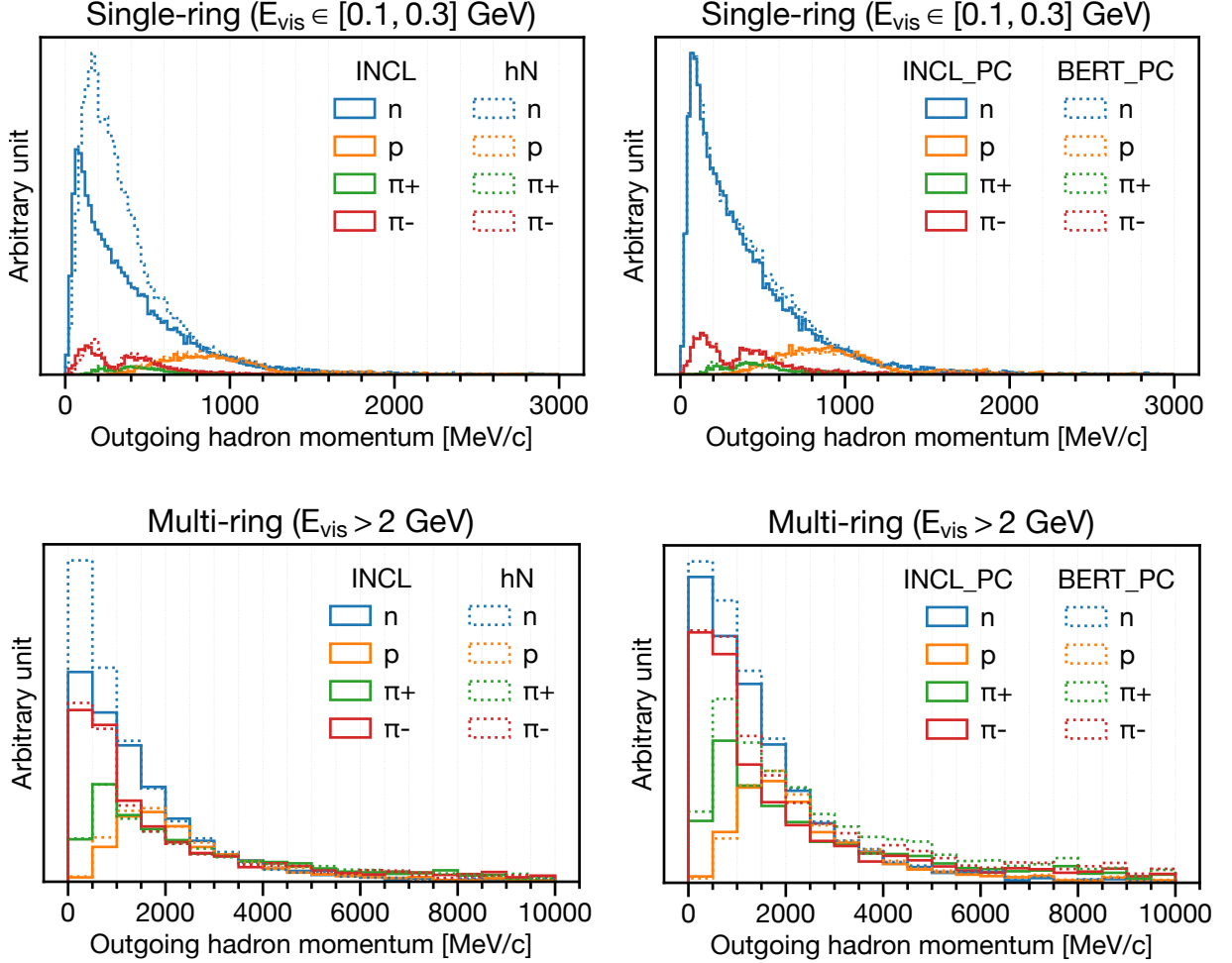


FIG. 25. Momentum distributions of outgoing hadrons predicted by neutrino event generators, weighted by the average  $(n, \gamma)$  multiplicity per projectile hadron momentum bin as predicted by secondary hadron-nucleus interaction models. The area under each histogram bin represents the average contribution of a specific hadron at a given momentum to the observable  $(n, \gamma)$  multiplicity. The top panels show predictions for single-ring events with visible energy ( $E_{\text{vis}}$ ) in the range  $[0.1, 0.3] \text{ GeV}$ , while the bottom panels correspond to multi-ring events with visible energy above  $2 \text{ GeV}$ . The left plots compare two different cascade models for final-state interactions (GENIE INCL and GENIE hN) coupled with the secondary hadron-nucleus interaction model G4 INCL\_PC, whereas the right plots compare two secondary interaction models (G4 INCL\_PC and G4 BERT\_PC) coupled with the neutrino event generator option GENIE hN.

- [1] P. Abratenko *et al.* (MicroBooNE collaboration), Phys. Rev. D **110**, 013006 (2024). 1185  
1186
- [2] M. Elkins *et al.* (MINERvA collaboration), Phys. Rev. D **100**, 052002 (2019). 1187  
1188
- [3] P. Abratenko *et al.* (MicroBooNE collaboration), The European Physical Journal C **84**, 1052 (2024). 1189  
1190
- [4] A. M. Ankowski, P. Coloma, P. Huber, C. Mariani, and E. Vagnoni, Phys. Rev. D **92**, 091301 (2015). 1191  
1192
- [5] C. L. Cowan, F. Reines, F. B. Harrison, H. W. Kruse, and A. D. McGuire, Science **124**, 103 (1956) 1193  
1194  
<https://www.science.org/doi/pdf/10.1126/science.124.3212.1192>
- [6] T. Wester *et al.* (Super-Kamiokande collaboration), Phys. Rev. D **109**, 072014 (2024). 1195  
1196
- [7] A. Takenaka *et al.* (Super-Kamiokande collaboration), Phys. Rev. D **102**, 112011 (2020). 1198  
1199
- [8] S. Agostinelli *et al.* (Geant4 collaboration), Nucl. Instrum. Methods A **506**, 250 (2003). 1200  
1201
- [9] J. Allison *et al.*, IEEE Transactions on Nuclear Science **53**, 270 (2006). 1202  
1203
- [10] J. Allison *et al.*, Nucl. Instrum. Methods A **835**, 186 (2016). 1204  
1205
- [11] J. Cugnon, Nucl. Phys. A **387**, 191 (1982). 1206
- [12] J.-C. David *et al.*, Progress In Nuclear Science and Technology **2**, 942 (2011). 1207  
1208
- [13] R. Akutsu, A study of neutrons associated with neutrino and antineutrino interactions on the water target at the T2K far detector, Ph.D. thesis, The Univ. of Tokyo (2019). 1209  
1210  
1211  
1212
- [14] B. Aharmim *et al.* (SNO collaboration), Phys. Rev. D **99**, 112007 (2019). 1213  
1214
- [15] A. Olivier *et al.* (MINERvA collaboration), Phys. Rev. D **108**, 112010 (2023). 1215  
1216
- [16] S. Abe *et al.* (KamLAND Collaboration), Phys. Rev. D **107**, 072006 (2023). 1217  
1218
- [17] S. Sakai *et al.* (Super-Kamiokande Collaboration), Phys. Rev. D **109**, L011101 (2024). 1219  
1220
- [18] M. B. Chadwick *et al.*, Nuclear Data Sheets **112**, 2887 (2011), special Issue on ENDF/B-VII.1 Library. 1221  
1222  
1223
- [19] K. Abe *et al.* (Super-Kamiokande collaboration), Nucl. Instrum. Methods A **1027**, 166248 (2022). 1223  
1224
- [20] K. Abe *et al.*, Nuclear Instruments and Methods in Physics Research Section A: Accelerators, Spectrometers, Detectors and Associated Equipment **1065**, 169480 (2024). 1225  
1226  
1227
- [21] S. Fukuda *et al.* (Super-Kamiokande collaboration), Nucl. Instrum. Methods A **501**, 418 (2003). 1229  
1230
- [22] K. Abe *et al.*, Nucl. Instrum. Methods A **737**, 253–272 (2014). 1231  
1232
- [23] S. Yamada *et al.*, IEEE Trans. Nucl. Sci. **57**, 428 (2010) 1233
- [24] C. Andreopoulos *et al.*, Nucl. Instrum. Methods A **614**, 87 (2010), arXiv:0905.2517 [hep-ph]. 1234  
1235
- [25] C. Andreopoulos *et al.*, The GENIE Neutrino Monte Carlo Generator: Physics and User Manual (2015) 1236  
1237  
1238  
arXiv:1510.05494 [hep-ph].
- [26] J. Tena-Vidal *et al.* (GENIE), Phys. Rev. D **104**, 072009 (2021), arXiv:2104.09179 [hep-ph]. 1239  
1240
- [27] M. Shiozawa, Nucl. Instrum. Methods A **433**, 240 (1999) 1241
- [28] M. Honda, T. Kajita, K. Kasahara, and S. Midorikawa, Phys. Rev. D **83**, 123001 (2011). 1242  
1243
- [29] R. L. Workman *et al.* (Particle Data Group), PTEP **083C01**, 729 (2022). 1244  
1245
- [30] Y. Hayato and L. Pickering, Eur. Phys. J Spec. Top. **230**, 4469–4481 (2021). 1246
- [31] L. L. Salcedo, E. Oset, M. J. Vicente-Vacas, and C. Garcia-Recio, Nucl. Phys. A **484**, 557 (1988). 1247
- [32] E. S. P. Guerra *et al.*, Phys. Rev. D **99**, 052007 (2019). 1248
- [33] H. W. Bertini, Phys. Rev. **131**, 1801 (1963). 1249
- [34] P. de Perio, AIP Conf. Proc. **1405**, 223 (2011), arXiv:1405.3973 [nucl-ex]. 1250
- [35] A. M. Ankowski, O. Benhar, T. Mori, R. Yamaguchi, and M. Sakuda, Phys. Rev. Lett. **108**, 052505 (2012). 1251
- [36] H. Ejiri, Phys. Rev. C **48**, 1442 (1993). 1252
- [37] C. Zeitnitz and T. A. Gabriel, Nucl. Instrum. Meth. A **349**, 106 (1994). 1253
- [38] R. Brun, F. Bruyant, M. Maire, A. C. McPherson, and P. Zanarini, *GEANT3*, Tech. Rep. (CERN, 1987). 1254
- [39] H. W. Bertini, Phys. Rev. **188**, 1711 (1969). 1255
- [40] P. F. Rose, *ENDF-201: ENDF/B-VI summary documentation*, Tech. Rep. (Brookhaven National Lab. (BNL), Upton, NY (United States), 1991). 1256
- [41] E. Mendoza and D. Cano-Ott, *Update of the Evaluated Neutron Cross Section Libraries for the Geant4 Code (see also INDC(NDS)-0612)*, Tech. Rep. (International Atomic Energy Agency (IAEA), International Atomic Energy Agency (IAEA), 2018) iNDc(NDS)-0758. 1257
- [42] K. Hagiwara *et al.*, Prog. Theor. Exp. Phys. **2019**, 023D01 (2019), <https://academic.oup.com/ptep/article-pdf/2019/2/023D01/27970473/ptz002.pdf>. 1258
- [43] T. Tanaka *et al.*, Prog. Theor. Exp. Phys. **2020**, 043D02 (2020), <https://academic.oup.com/ptep/article-pdf/2020/4/043D02/33040537/ptaa015.pdf>. 1259
- [44] V. Barger, K. Whisnant, S. Pakvasa, and R. J. N. Phillips, Phys. Rev. D **22**, 2718 (1980). 1260
- [45] M. Jiang *et al.* (Super-Kamiokande collaboration), Progress of Theoretical and Experimental Physics **2019**, 053F01 (2019), <https://academic.oup.com/ptep/article-pdf/2019/5/053F01/28638877/ptz015.pdf>. 1261
- [46] A. M. Dziewonski and D. L. Anderson, Physics of the Earth and Planetary Interiors **25**, 297 (1981). 1262
- [47] K. Abe *et al.* (Super-Kamiokande collaboration), J. Instrum. **17** (10), P10029. 1263
- [48] F. Chollet *et al.*, Keras, <https://keras.io> (2015). 1264
- [49] K. He, X. Zhang, S. Ren, and J. Sun, Delving deep into rectifiers: Surpassing human-level performance on imagenet classification (2015), arXiv:1502.01852 [cs.CV]. 1265
- [50] D. P. Kingma and J. Ba, Adam: A method for stochastic optimization (2017), arXiv:1412.6980 [cs.LG]. 1266
- [51] H. Ito, K. Wada, T. Yano, Y. Hino, Y. Ommura, M. Harada, A. Minamino, and M. Ishitsuka, Nucl. Instrum. Methods A **1057**, 168701 (2023). 1267
- [52] S. Han, Measurement of neutrons produced in atmospheric neutrino interactions at super-kamiokande, Ph.D. thesis, The Univ. of Tokyo (2024). 1268
- [53] Y. Hino, K. Abe, R. Asaka, S. Han, M. Harada, M. Ishitsuka, H. Ito, S. Izumiya, Y. Kanemura, Y. Koshio, F. Nakanishi, H. Sekiya, and T. Yano, Progress of Theoretical and Experimental Physics **2025**, 013C01 (2024), <https://academic.oup.com/ptep/article-pdf/2025/1/013C01/61281853/ptae193.pdf>. 1269
- [54] B. Pritychenko and S. F. Mughabghab, Nuclear Data Sheets **113**, 3120 (2012). 1270
- [55] T. Hastie and R. Tibshirani, *Generalized Additive Mod-* 1271

- els, Chapman & Hall/CRC Monographs on Statistics & Applied Probability (Taylor & Francis, 1990). 1273
- [56] D. Servén, C. Brummitt, and H. Abedi, dswah/pygam v0.8.0 (2018). 1274
- [57] D. Wright and M. Kelsey, Nucl. Instrum. Methods A **804**, 175 (2015). 1275
- [58] D. Mancusi, A. Boudard, J. Cugnon, J.-C. David, P. Kai taniemi, and S. Leray, Phys. Rev. C **90**, 054602 (2014). 1276
- [59] A. Kelic, M. V. Ricciardi, and K.-H. Schmidt, Abla07 towards a complete description of the decay channels of a nuclear system from spontaneous fission to multifragmentation (2009), arXiv:0906.4193 [nucl-th]. 1277
- [60] J. Quesada Molina *et al.*, Progress in Nuclear Science and Technology **2**, 936 (2011). 1278
- [61] V. M. Grichine, The European Physical Journal C **62**, 399 (2009). 1279
- [62] V. Weisskopf, Phys. Rev. **52**, 295 (1937). 1280
- [63] I. Dostrovsky, Z. Fraenkel, and G. Friedlander, Phys. Rev. **116**, 683 (1959). 1281
- [64] A. Chatterjee, K. H. N. Murthy, and S. K. Gupta, Pramana **16**, 391 (1981). 1282
- [65] C. Kalbach, Preco-2000, exciton model preequilibrium code system with direct reactions. preco-d2, pre-equilibrium and direct reaction double differential cross-sections (2002). 1283
- [66] A. Boudard and J. Cugnon, Incl4 - the liège inc model for high-energy hadron-nucleus reactions: A short decription of the incl4.2 and incl4.4 versions (2008). 1284
- [67] A. Boudard, J. Cugnon, J.-C. David, S. Leray, and D. Mancusi, Phys. Rev. C **87**, 014606 (2013). 1285
- [68] A. Ershova *et al.*, Phys. Rev. D **106**, 032009 (2022). 1286
- [69] D. Mancusi *et al.*, The European Physical Journal A **53**, 80 (2017). 1287
- [70] T. Aoust and J. Cugnon, Phys. Rev. C **74**, 064607 (2006). 1288
- [71] S. Dytman, Y. Hayato, R. Raboanary, J. T. Sobczyk, J. Tena-Vidal, and N. Vololonaina, Phys. Rev. D **104**, 053006 (2021). 1289
- [72] Y. Ashida, H. Nagata, M. Mori, G. Collazuol, D. Fukuda, T. Horai, F. Iacob, A. Konaka, Y. Koshio, T. Nakaya, C. Nantais, T. Shima, A. Suzuki, Y. Takeuchi, H. Tanaka, R. Wendell, and T. Yano, Phys. Rev. C **109**, 014620 (2024). 1290
- [73] T. Tano, T. Horai, Y. Ashida, Y. Hino, F. Iacob, A. Maurel, M. Mori, G. Collazuol, A. Konaka, Y. Koshio, T. Nakaya, T. Shima, and R. Wendell, Progress of Theoretical and Experimental Physics **2024**, 113D01 (2024), <https://academic.oup.com/ptep/article-pdf/2024/11/113D01/60833777/ptae159.pdf>. 1291
- [74] Y. Hino, A comparison of n-o inelastic scattering between the experimental and simulation models towards understanding neutrino reaction (2024). 1292
- [75] M. Smy, in *International Cosmic Ray Conference*, International Cosmic Ray Conference, Vol. 5 (2008) pp. 1279–1282. 1293